(2)

ARMY RESEARCH LABORATORY

Projectile Base Bleed Technology Part I: Analysis and Results

Howard J. Gibeling
Richard C. Buggeln

ARL-CR-2 November 1992

prepared by

Scientific Research Associates, Inc.
50 Nye Road
P.O. Box 1058
Glastonbury, CT 06033

under contract

DAA15-88-C-0040

NOTICES

Destroy this report when it is no longer needed. DO NOT return it to the originator.

Additional copies of this report may be obtained from the National Technical Information Service, U.S. Department of Commerce, 5285 Port Royal Road, Springfield, VA 22161.

The findings of this report are not to be construed as an official Department of the Army position, unless so designated by other authorized documents.

The use of trade names or manufacturers' names in this report does not constitute indorsement of any commercial product.

REPORT DOCUMENTATION PAGE

Form Approved
OMB No. 0704-0188

1. AGENCY USE ONLY (Leave blank)	2. REPORT DATE	3. REPORT TYPE AND DATES COVERED
	November 1992	Final, July 1988 - July 1991

4. TITLE AND SUBTITLE

PROJECTILE BASE BLEED TECHNOLOGY; PART I: ANALYSIS AND RESULTS

5. FUNDING NUMBERS

DAA15-88-C-0040

6. AUTHOR(S)

HOWARD J. GIBELING and RICHARD C. BUGGELN

7. PERFORMING ORGANIZATION NAME(S) AND ADDRESS(ES)

Scientific Research Associates, Inc.
50 Nye Road, P.O. Box 1058
Glastonbury, CT 06033

8. PERFORMING ORGANIZATION REPORT NUMBER

R91-930020-F

9. SPONSORING/MONITORING AGENCY NAME(S) AND ADDRESS(ES)

U.S. Army Research Laboratory
ATTN: AMSRL-OP-CI-B (Tech Lib)
Aberdeen Proving Ground, MD 21005-5066

10. SPONSORING/MONITORING AGENCY REPORT NUMBER

ARL-CR-2

11. SUPPLEMENTARY NOTES

The Contracting Officer's Representative for this report is Charles J. Nietubicz, U.S. Army Research Laboratory, ATTN: AMSRL-WT-PB, Aberdeen Proving Ground, MD, 21005-5066.

12a. DISTRIBUTION/AVAILABILITY STATEMENT

Approved for public release; distribution is unlimited.

12b. DISTRIBUTION CODE

13. ABSTRACT *(Maximum 200 words)*

Detailed finite rate chemistry models for H_2 and H_2-CO combustion have been incorporated into a Navier-Stokes computer code and applied to flow field simulation in the base region of an M864 base burning projectile. Results without base injection were obtained using a low Reynolds number k-ε turbulence model and several mixing length turbulence models. The results with base injection utilized only the Baldwin-Lomax model for the projectile forebody and the Chow wake mixing model downstream of the projectile base.

A validation calculation was performed for a supersonic hydrogen-air burner using an H_2 reaction set which is a subset of the H_2-CO reaction set developed for the base combustion modeling. The comparison with the available experimental data was good, and provides a level of validation for the technique and code developed. Projectile base injection calculations were performed for a flat base M864 projectile at $M_\infty = 2$. Hot air injection, H_2 injection and H_2-CO injection were modeled, and computed results show reasonable trends in the base pressure increase (base drag reduction), base corner expansion and downstream wake closure location.

14. SUBJECT TERMS

Projectile Base Combustion
Hydrogen Combustion
Hydrogen-Carbon Monoxide Combustion
Projectile Base Drag
Navier-Stokes Base Flow Analysis
Combustion
Projectiles

15. NUMBER OF PAGES

82

16. PRICE CODE

17. SECURITY CLASSIFICATION OF REPORT	18. SECURITY CLASSIFICATION OF THIS PAGE	19. SECURITY CLASSIFICATION OF ABSTRACT	20. LIMITATION OF ABSTRACT
UNCLASSIFIED	UNCLASSIFIED	UNCLASSIFIED	UL

INTENTIONALLY LEFT BLANK.

TABLE OF CONTENTS

Intentionally left blank.

LIST OF FIGURES

LIST OF TABLES

Intentionally left blank.

ACKNOWLEDGEMENTS

The authors would like to thank Dr. Olin Jarrett, Jr. of NASA Langley Research Center for providing the supersonic burner experimental data, Mr. Melvin Steinle of Talley Defense Systems for providing details on the propellant for the M864 base burn projectile, and Dr. Walter B. Sturek, Charles J. Nietubicz, and James E. Danberg of the Ballistic Research Laboratory for many fruitful discussions as well as data, grids and computed results for comparison with present calculations.

Intentionally Left Blank

PREFACE

The U.S. Army Ballistic Research Laboratory was deactivated on 30 September 1992 and subsequently became a part of the U.S. Army Research Laboratory (ARL) on 1 October 1992.

INTENTIONALLY LEFT BLANK.

1. INTRODUCTION

The subject of the flow behind a projectile in flight has been studied extensively for many years. Since the drag on the projectile due to the reduced pressure on the base is a significant portion of the total drag, aerodynamicists have devised various methods for reducing the "base drag". An important technique for reducing the base drag (i.e., increasing the base pressure) is the injection of combustible gases from the base. These gases subsequently mix with the free stream air and burn downstream of the projectile. This method for reducing drag was first suggested many decades ago (e.g., Baker, Davis and Matthews 1951). A collection of papers on analytic and experimental studies of base combustion was edited by Murthy et al. (1976). This work also includes a review of base flow phenomena with and without injection by Murthy and Osborn (1976) through 1974. Numerous approximate techniques for analysis of the base combustion flow problem, and the influence on base drag were presented. Strahle and his co-workers, (Hubbartt, Strahle and Neale 1981 and Strahle, Hubbartt and Walterick 1982), have experimentally studied base burning and external burning in supersonic flow using H_2 and diluents. The effect of injectant molecular weight and energy content on base drag was investigated.

The increase in capability for analyzing complicated flow problems using computational fluid dynamics (CFD) techniques, and the availability of super computers have led to improved numerical analysis of both forebody and base flow problems. Sturek, Nietubicz, Sahu, Danberg and others (Sturek et al. 1978; Nietubicz, Inger and Danberg 1984; Sahu, Nietubicz and Steger 1985; Sahu 1986; and Sahu and Danberg 1986) from the U.S. Army Ballistic Research Laboratory have utilized inviscid/boundary-layer coupled techniques and implicit Navier-Stokes codes (Nietubicz, Pulliam and Steger 1980) to study the flow fields for many different projectile configurations. These works have considered base flows without injection as well as with injection of cold or hot air. Sahu and Nietubicz (1984) and Childs and Caruso (1987) have also considered the base flow problem with a propulsive jet. However, the present work concentrates on the so-called base bleed phenomena in which only a relatively small mass of gas is injected from the base.

Modern U.S. Army projectiles utilize injection gases generated by burning a fuel rich solid propellant whose primary combustion products are H_2, CO, HCl and other noncombustible gases. These injection gases exit the projectile base at low speed relative to the initial flight speed, and the duration of injection is of order 30 seconds. No detailed analysis technique has been developed yet for the base flow combustion

problem. The present effort develops several combustion models suitable for inclusion in Navier-Stokes computational procedures for projectile base flow field prediction. These models have evolved from the hydrogen-air combustion literature for scramjet and ramjet reacting flow problems, and from the hydrocarbon combustion literature.

Hydrogen combustion has been studied extensively for many years. For example, Spiegler, Wolfshtein and Manheimer-Timnat (1976) utilized a seven species, eight reaction model including the influence of turbulent fluctuations. Janicka and Kollmann (1979) proposed a two-scalar formulation based on a seven reaction system and a two-dimensional pdf for modeling the effect of turbulence in an H_2-air diffusion flame. This model assumes that the two-body "shuffle" reactions occur very rapidly so that they are in equilibrium, while the slower three-body recombination reactions are considered kinetically.

Rogers and Chinitz (1983) developed a two-step global reaction model for H_2-air combustion at one atmosphere pressure. This model requires only five species including N_2; therefore, it is more efficient than the more extensive mechanisms. Also, this model includes the effect of stoichiometry on the global reaction rates. Uenishi, Rogers and Northam (1987) used the Rogers and Chinitz model successfully for three-dimensional predictions behind a back-step in a supersonic combustor. More recently, Jachimowski (1988) developed a 13 species, 33 reaction model for H_2-air combustion studies in hypersonic flows over a range of initial temperatures. A nine species, 18 reaction model was also proposed by Jachimowski (1988).

Evans and Schexnayder (1980) used the Spiegler, Wolfshtein and Manheimer-Timnat (1976) reaction system and a 12 species, 25 reaction system along with the "unmixedness" formulation of Spiegler to compare with several different supersonic flame test cases. The important conclusions from this study were that the 25 reaction system was superior to the eight reaction system for the prediction of ignition, but that otherwise the eight reaction system was acceptable. Unmixedness also had a significant influence in one case where ignition failed to occur; otherwise, the effect was moderate. Eklund, Drummond and Hassan (1990) used a modified seven reaction set patterned after that of Jachimowski (1988) to calculate the combustion in turbulent shear layers and compare with experimental data.

The consideration of H_2 and CO in flames has not been as extensive as hydrogen alone. Early work was performed at Princeton University by Dryer (1972) and Dryer and Glassman (1973) in both carbon monoxide and methane oxidation. Westbrook et al. (1977) developed a detailed finite rate model to analyze the experimental results of Dryer and Glassman. The resulting mechanism consisted of 19 species and 56 reactions

which was validated for the temperature range 1000-1350 K. A subset of this reaction set was presented by Dryer and Glassman (1978) for H_2-CO oxidation. Correa et al. (1984) presented a partial equilibrium model for a turbulent CO-H_2-N_2 coaxial jet reacting with air at atmospheric pressure. The model was an extension of the two-scalar pdf approach of Janicka and Kollmann (1979) to include CO in the radical pool. White, Drummond and Kumar (1987) used a double flame sheet model for temperatures below 2500 K in a dual combustor ramjet analysis which considered H_2 and CO in the fuel. Above 2500 K a chemical equilibrium calculation was performed. The solution procedure was based on an explicit forward marching boundary-layer approach.

The first phase of the present effort, involved application of the CMINT computer code (Scientific Research Associates 1991) to both the projectile forebody flow and the projectile base flow analysis both with and without injection. Both an algebraic mixing length and a two-equation k-ϵ turbulence model were employed in the initial studies. The Baldwin-Lomax (1978) model as described by Sahu and Danberg (1986) was subsequently implemented for the projectile forebody turbulence model, and a wake mixing model due to Chow (1985) was used downstream of the projectile base.

Subsequently, several combustion models which are applicable to the projectile base burning flow problem were developed. Application of these models demonstrates the effect of base region burning on the projectile base pressure. In addition to these projectile flows, a validation calculation was performed for comparison with the experimental data of Jarrett et al. (1988) on a supersonic burner (SSB) using H_2 fuel.

2. ANALYSIS

The present combustion model development effort focused on finite rate reaction models which were general enough to encompass the flow conditions encountered throughout the flight regime of current and proposed Army base burning projectiles. Since the flow behind a projectile contains recirculation zones, the reaction schemes considered must be suitable for inclusion in a Navier-Stokes analysis. An implicit numerical procedure is desirable because of both the presence of thin shear layers and the probable stiff nature of the equations due to the chemical source terms in the species conservation equations.

2.1 Governing Equations. The equations describing the viscous, chemically reacting projectile base flow are the ensemble-averaged Navier-Stokes equations coupled with the species conservation and turbulence model equations. The mean flow equations are obtained by using mass-weighted (Favre) averages of the dependent variables. For the present application these equations are written in a nonorthogonal body-fitted, cylindrical coordinate system. The governing partial differential equations were formulated in conservation form by application of a Jacobian transformation to the equations in cylindrical coordinates. An outline of the transformation as well as the transformed system of equations is given in Appendix A. The vector form of the equations is described below.

The continuity equation is written as

$$\frac{\partial \rho}{\partial t} + \nabla \cdot (\rho \mathbf{U}) = 0 \tag{1}$$

The momentum conservation equation is

$$\frac{\partial (\rho \mathbf{U})}{\partial t} + \nabla \cdot (\rho \mathbf{U}\mathbf{U}) = -\nabla p + \nabla \cdot \tau \tag{2}$$

where τ is the stress tensor (molecular and turbulent) given by

$$\tau_{ij} = 2\mu_{eff}\, e_{ij} - \frac{2}{3}\, \mu_{eff}\, \nabla \cdot \mathbf{U}\, \delta_{ij} \tag{3}$$

and the rate of strain tensor, e_{ij} is given by

$$e_{ij} = \frac{1}{2}\left[\frac{\partial U_i}{\partial x_j} + \frac{\partial U_j}{\partial x_i} \right] \tag{4}$$

The effective viscosity, μ_{eff}, is the sum of the molecular and turbulent viscosities

$$\mu_{eff} = \mu + \mu_T \tag{5}$$

The turbulent viscosity, μ_T, is obtained from the turbulence model.

The energy conservation equation is written in terms of the stagnation enthalpy, h_o, as

$$\frac{\partial (\rho h_o)}{\partial t} + \nabla \cdot (\rho \mathbf{U} h_o) = \frac{\partial p}{\partial t} - \nabla \cdot \mathbf{q} + \nabla \cdot (\tau \cdot \mathbf{U}) \tag{6}$$

where the last term in Eq. (6) is the stress work and $\mathbf{q}$ is the multicomponent energy flux vector consisting of the Fourier heat flux and interdiffusional energy flux $\mathbf{q}_d$,

$$\mathbf{q} = - \kappa_{eff} \nabla T + \mathbf{q}_d \tag{7}$$

where κ_{eff} is the effective thermal conductivity. In the present analysis, κ_{eff} is obtained assuming constant molecular and turbulent Prandtl numbers, Pr and Pr_T, i.e.

$$\kappa_{eff} = \frac{\mu C_p}{Pr} + \frac{\mu_T C_p}{Pr_T} \tag{8}$$

The interdiffusional energy flux is given by

$$\mathbf{q}_d = \sum_{i=1}^{N_s} h_i(T)\ \mathbf{j}_i \tag{9}$$

where $\mathbf{j}_i$ is defined in Eq. (12) and $h_i(T)$, the enthalpy of species i per unit mass, is

$$h_i(T) = h_{fi} + \int_{T_f}^{T} C_{pi}(T')dT' \tag{10}$$

The species conservation equations are expressed as

$$\frac{\partial(\rho Y_i)}{\partial t} + \nabla\cdot(\rho \mathbf{U} Y_i) = - \nabla\cdot\mathbf{j}_i + m_i \tag{11}$$

where Y_i is the mass fraction of species i, m_i is rate of production of species i due to chemical reaction, and $\mathbf{j}_i$ is the diffusional mass flux of species i. Assuming that the diffusion of mass is governed by Fick's law, $\mathbf{j}_i$ is given by

$$\mathbf{j}_i = - \rho D \nabla Y_i \tag{12}$$

where D is the diffusion coefficient (independent of species i) which is obtained by assuming constant molecular and turbulent Schmidt numbers, Sc and Sc_T, i.e.

$$\rho D = \frac{\mu}{Sc} + \frac{\mu_T}{Sc_T} \tag{13}$$

Finally, for a mixture of perfect gases the equation of state is

$$p = \rho RT \tag{14}$$

$$R = R_u \sum_{i=1}^{N_s} \frac{Y_i}{W_i}$$

where R_u is the universal gas constant, W_i is the molecular weight of species i, and N_s is the total number of species in the system. The caloric equation of state relates the temperature and the static enthalpy as

$$h = \sum_{i=1}^{N_s} Y_i \, h_i(T) \tag{15}$$

This relation is evaluated using the JANNAF database of polynomial curve fit coefficients for C_{pi} and h_i as functions of T which are available from NASA Lewis Research Center (Gordon and McBride 1976).

2.2 General Chemistry Model. The typical solid propellant used in base burning projectiles is a fuel rich mixture which yields combustion products consisting primarily of H_2, CO, HCl, CO_2, H_2O and N_2. The mole fractions of these constituents in chemical equilibrium sum to 0.997, hence there is little error in ignoring the remaining trace species. Since the available energy in the HCl is relatively small compared to that of H_2 and CO, the HCl has been replaced by a combination of CO, CO_2 and N_2. Both the heat of combustion and the molecular weight of the equivalent mixture were matched to those of the original equilibrium combustion products. The composition of this equivalent mixture is given in Table I.

As the base injectant gas mixes with the free stream air, further reaction takes place in the region near the projectile base. Exactly where the combustion occurs is a function of the injectant gas temperature, the mass and momentum flow rates, the degree of turbulent mixing, the effect of turbulent fluctuations and the rates of the important chemical reactions. In the absence of turbulence, the reaction rates are fairly well known for the H_2-CO system; however, there are still some uncertainties which must be recognized in evaluating the results. The sensitivity of the reaction rate coefficients to pressure (e.g., Gardiner 1984) does not appear to be significant for the range of pressures encountered in the projectile base flow problem.

The injectant gas temperature can be calculated if it is assumed that the solid propellant combustion products are in chemical equilibrium upon exiting the projectile

base. However, available thermocouple measurements of the temperature in the combustion chamber of a typical Army projectile (Kayser, Kuzan and Vasquez 1987) indicate a temperature ($T_{inj} \sim 1500$ K) about 500 K lower than the predicted adiabatic equilibrium flame temperature obtained using the NASA Lewis CET86 code (Gordon and McBride 1976). Therefore, in the present analysis the composition of the injectant gas was determined by assuming that the products were in equilibrium at the experimentally observed temperature. It should be noted that the differences between the compositions in these two situations were not large. Hence, an important factor regarding the injection conditions is simply the correct specification of the injectant gas temperature because of its direct influence on base pressure.

In general reactions are of the form

$$\sum_{i=1}^{\ell} \nu'_{i,r} X_i \underset{k_{b,r}}{\overset{k_{f,r}}{\rightleftharpoons}} \sum_{i=1}^{\ell} \nu''_{i,r} X_i \tag{16}$$

where $\nu'_{i,r}$ and $\nu''_{i,r}$ are the stoichiometric coefficients appearing on the left and right of the reaction r and $k_{f,r}$ and $k_{b,r}$ are the forward and backward rate constants and $[X_i]$ is the molar concentration of any species X_i. It can be shown (e.g., Vincenti and Kruger 1965) that the rate of production of species i in reaction r is given by

$$\left[\frac{d[X_i]}{dt}\right]_r = \left(\nu''_{i,r} - \nu'_{i,r}\right) k_{f,r} \prod_{s=1}^{\ell} [X_s]^{\nu'_{s,r}}$$

$$+ \left(\nu'_{i,r} - \nu''_{i,r}\right) k_{b,r} \prod_{s=1}^{\ell} [X_s]^{\nu''_{s,r}} \tag{17}$$

where the forward and backward reaction rates are related by the equilibrium constant, $K_{c,r}$, viz.,

$$K_{c,r} = \frac{k_{f,r}}{k_{b,r}} \tag{18}$$

Reaction rates for the models considered herein are expressed in the Arrhenius form, i.e.,

$$k_{f,r} = A_r T^{b_r} \exp\left[-\frac{E_r}{R_u T}\right] \tag{19}$$

where R_u is the universal gas constant, and E_r is the activation energy of reaction r.

The equilibrium constant is actually a function of temperature and is given by the relationship (Vincenti and Kruger 1965),

$$K_{c,r} = \frac{\exp\left[-\frac{\left[\sum\left(\nu''_{i,r} - \nu'_{i,r}\right)\hat{\mu}^{o}_{i}\right]}{R_u T}\right]}{R_u T^{\sum\left(\nu''_{i,r} - \nu'_{i,r}\right)}} \tag{20}$$

where $\hat{\mu}^{o}_{i}$ is given by

$$\hat{\mu}^{o}_{i}(T) = \int_{T_o}^{T} \hat{c}_{p_i}\, dT + \hat{h}^{o}_{i} - T\left[\int_{T_o}^{T} \frac{\hat{c}_{p_i}}{T}\, dT + \hat{s}^{o}_{i}\right] - R_u \ln p_o \tag{21}$$

where $\hat{h}^{o}_{i}$ and $\hat{s}^{o}_{i}$ are the enthalpy and entropy per mole at the reference conditions T_o and p_o. The quantity $\hat{\mu}^{o}_{i}$ is the chemical potential (Gibbs free energy per mole) for a pure species at unit pressure. Eqs. (18) - (21) enable the calculation of both the forward and backward rate constants, provided that the constants k_{fr}, A_r, b_r and E_r are known for each reaction, and Eq. (17) represents the rate source term for each species. Since the species equations are written with the mass fractions as the dependent variables, the molar concentrations are related to the mass fractions by

$$[X_i] = \frac{\rho Y_i}{W_i} \tag{22}$$

Thus, the source terms due to both forward and backward reactions can be expressed in terms of the dependent variables: the three velocity components, the density, the stagnation enthalpy, and the mass fraction; and can be appropriately linearized for implicit treatment. The influence of both concentration fluctuations on the chemical production rates and temperature fluctuations on the Arrhenius rate expressions has been neglected in this study.

The ignition of the injectant gas should be quite rapid under projectile base injection conditions at projectile launch, since the temperature is high and the pressure is near one-half atmosphere; therefore reaction mechanisms that properly model the

chemistry of the ignition process may not required. The sensitivity of the analysis to the initial base pressure must be investigated for extremes in the initial flight conditions. The first mechanism considered for CO oxidation is due to Westbrook et al. (Dryer and Glassman 1978); however, the rates presented may not be valid for temperatures in excess of 1350 K. Therefore, rates have been selected from the work edited by Gardiner (1984) wherever possible. The modified model reactions and the Arrhenius constants for the forward reactions are shown in Table II for reaction set A. This set consists of 23 reactions involving nine primary species H_2, O_2, OH, H_2O, O, H, CO, CO_2, and N_2 in addition to two secondary species HO_2 and H_2O_2; this set should permit the calculation of ignition and the evaluation of its importance for projectile base combustion flows.

Since the initial results for the base combustion problem with set A indicated very rapid ignition due to the high initial injection temperature, a reduced set of species and reactions could be considered. The effect of reaction set A on the projectile base drag may be neglected compared to the reduced reactions sets considered under this study since a maximum change of 0.002 in C_{DB} values was observed. The reactions comprising set B are the first 12 reactions involving the nine primary species. The first eight reactions in Table II are the same as the Spiegler, Wolfshtein and Manheimer-Timnat (1976) reaction set. Reaction number nine was also used by Eklund, Drummond and Hassan (1990), but the rate proposed by Westbrook et al. (1977) is much larger than that used by Eklund, Drummond and Hassan (1990). In addition, the work of Gardiner (1984) quotes a rate between the latter two, but with unspecified products of reaction. The importance of this reaction has been assessed for the present applications.

2.3 Global Hydrogen - Air Combustion Model. In the case of pure H_2 combustion in air, some simplification of the finite rate chemistry model is possible under certain circumstances. When the prediction of ignition is not a critical factor, say due to high initial temperatures, then the Rogers and Chinitz (1983) two-step global reaction model is very attractive. This model requires only five species including N_2; hence, it is more efficient than the detailed reaction mechanisms. The model is strictly applicable only for combustion at one atmosphere pressure and the effect of stoichiometry on the global reaction rates is included. This model was selected for the base combustion calculation in order to demonstrate a simpler reaction set than that for H_2-CO combustion. The applicability of the model is assessed by comparison with other base combustion model results.

The reactions for the Rogers and Chinitz model are:

$$H_2 + O_2 \underset{k_{b_1}}{\overset{k_{f_1}}{\rightleftharpoons}} 2OH \tag{23}$$

and

$$2OH + H_2 \underset{k_{b_2}}{\overset{k_{f_2}}{\rightleftharpoons}} 2H_2O \tag{24}$$

where in this form the Arrhenius equation is

$$k_{f_i} = A_i(\phi)T^{b_i}\, e^{-E_i/R_uT} \tag{25}$$

where ϕ is the equivalence ratio for the overall reaction process. For the first reaction

$$\begin{aligned} A_1(\phi) &= (8.917\phi + 3.433/\phi - 28.950) \times 10^{47} \\ E_1 &= 4865 \text{ cal/mole} \\ b_1 &= -10 \end{aligned} \tag{26}$$

The dimensions of k_{f_1} are cm^3/mole-sec. For the second reaction

$$\begin{aligned} A_2(\phi) &= (2.000 + 1.333/\phi - 0.833\phi) \times 10^{64} \\ E_2 &= 42{,}500 \text{ cal/mole} \\ b_2 &= -13 \end{aligned} \tag{27}$$

The dimensions of k_{f_2} are $cm^6/mole^2$-sec. The equivalence ratio is defined as:

$$\phi = \frac{(F/O)}{(F/O)_{st}} \tag{28}$$

where (F/O) is the fuel to oxidizer ratio by mass.

For the reaction set of Eq. (23) and Eq. (24)

$$(F/O)_{st} = \frac{1}{8}$$

$$\phi = \frac{Y_{H_2}/Y_{O_2}}{1/8} \tag{29}$$

2.4 Turbulence Models. Both an algebraic mixing length model and a two-equation k-ϵ model due to Jones and Launder (1972) were previously included in the CMINT code. In addition, the Baldwin-Lomax (1978) model as described by Sahu and Danberg (1986) was implemented for the projectile forebody turbulence model, and a wake mixing model due to Chow (1985) was used downstream of the projectile base. The k-ϵ model was evaluated in some preliminary base flow calculations.

The approach taken in these models assumes an isotropic turbulent viscosity, μ_T, and relates the Reynolds stress tensor to the mean flow gradients, viz.

$$-\rho\,\overline{u_i' u_j'} = \mu_T \left[2e_{ij} - \frac{2}{3}\nabla\cdot U\,\delta_{ij}\right] \tag{30}$$

where e_{ij} is given in Eq. (4).

2.4.1 Algebraic Mixing Length Model. In the mixing length model the turbulent viscosity is determined from

$$\mu_T = \rho \ell^2 \left[2e_{ij}e_{ij}\right]^{\frac{1}{2}} \tag{31}$$

and the mixing length is obtained from the Van Driest formulation with a free stream length scale ℓ_∞.

$$\ell_\infty = 0.09\,\delta \tag{32}$$

where δ is the local boundary layer thickness. The mixing length is given by

$$\ell = D_\ell \cdot \ell_\infty \tanh\left[\frac{\kappa y_n}{\ell_\infty}\right] \tag{33}$$

where y_n is the distance normal to the wall and κ is the von Karman constant, $\kappa = 0.4$.

The van Driest damping factor D_ℓ is

$$D_\ell = 1 - e^{-y^+/26} \tag{34}$$

where the wall coordinate y^+ is

$$y^+ = \frac{\rho u_\tau}{\mu} y_n \tag{35}$$

and the friction velocity is obtained from the wall shear, τ_w,

$$u_\tau = \left[\frac{\tau_w}{\rho_w}\right]^{\frac{1}{2}} \tag{36}$$

While this model gives acceptable results for turbulent viscosity on the projectile forebody, it does require determination of the boundary layer thickness. Thus, this model is not directly applicable to the base region turbulence.

2.4.2 Baldwin-Lomax Model. The present description of the so-called Baldwin-Lomax (1978) model was summarized by Sahu and Danberg (1986). First, an "inner" layer turbulent viscosity is defined by

$$(\mu_T)_{inner} = \rho \ell^2 |\vec{\omega}| \tag{37}$$

where the Van-Driest mixing length is given by

$$\ell = \kappa y_n D_\ell \tag{38}$$

and the damping factor is defined in Eq. (34). Also, $|\vec{\omega}|$ is the absolute value of the vorticity. The "outer" layer turbulent viscosity is defined by

$$(\mu_T)_{outer} = K\, C_{cp}\, \rho\, F_{wake}\, F_{kleb}(y) \tag{39}$$

where

$$F_{wake} = \min(y_{max} F_{max},\ C_{wk} y_{max} u^2_{diff} / F_{max})$$

$$F_{max} = \max[F(y)] = F(y_{max}) \tag{40}$$

$$F(y) = y_n |\vec{\omega}| D_\ell$$

and u_{diff} is the difference between the maximum and minimum velocities in a shear

layer. For a boundary layer, the above minimum velocity is zero. Also, the Van Driest damping factor is neglected in free shear layers and wakes. The constants used in the model are $\kappa = 0.4$, $C_{cp} = 1.6$, $C_{kleb} = 0.3$, $C_{wk} = 0.25$ and $K = 0.0168$.

2.4.3 Jones-Launder k-ϵ Model. The low Reynolds number k-ϵ model of Jones and Launder (1972) does not require the specification of a length scale or boundary layer thickness. One disadvantage of the model is the requirement for fine near wall resolution to resolve large gradients in the turbulence kinetic energy (k). Also, the equations contain ad hoc low turbulence Reynolds number correction terms. With the k-ϵ model the turbulent viscosity is obtained from the Prandtl-Kolmogorov relation,

$$\mu_T = C_\mu \frac{\rho k^2}{\epsilon} \tag{41}$$

The empirical constants σ_k, σ_ϵ and C_2 required in the k and ϵ transport equations (Appendix A) are taken from Jones and Launder (1972) and the constant C_1 from Launder and Spalding (1974), i.e.,

$$C_1 = 1.44 \tag{42a}$$

$$C_2 = 1.92 \left[1.0 - 0.3 \exp\left(-R_T^2\right)\right] \tag{42b}$$

$$C_\mu = 0.09 \exp\left[-\frac{2.5}{1 + R_T/50}\right] \tag{42c}$$

$$\sigma_k = 1.0 \tag{42d}$$

$$\sigma_\epsilon = 1.3 \tag{42e}$$

2.4.4 Eggers Turbulence Model. The Eggers (1971) algebraic mixing length model was developed for the nonreacting mixing of coaxial hydrogen-air jets. For the reacting coaxial jet experiment of Jarrett et al. (1988), this model was modified by Eklund, Drummond and Hassan (1990) to use the diatomic hydrogen profile to characterize the shear layer. The turbulent viscosity was defined as

$$\mu_T = C_e \rho U_{cl} R_l \tag{43}$$

where C_e is a constant (0.032), U_{cl} is the streamwise velocity on the jet centerline, and R_l is the width of the mixing layer. The width is defined as the radial distance between the

points in the profile where the H_2 mass fractions are $Y_1(H_2)$ and $Y_2(H_2)$,

$$Y_1(H_2) = Y_a(H_2) + 0.95\,[Y_o(H_2) - Y_a(H_2)]$$

$$Y_2(H_2) = Y_a(H_2) + 0.5\,[Y_o(H_2) - Y_a(H_2)] \qquad (44)$$

where $Y_a(H_2)$ is the H_2 mass fraction in the external outer jet flow and $Y_o(H_2)$ is the mass fraction of H_2 on the jet centerline.

2.5 Solution Technique. Solutions of the above equations were computed using a reacting flow version of SRA's Navier-Stokes code, CMINT. Centered spatial differences were used with adjustable artificial dissipation. The equations were solved using a linearized block implicit (LBI) algorithm and an ADI approximate factorization. A spatially varying time step was used to accelerate convergence to a steady solution. For the reacting flow solutions the time step for the coupled species equations was further conditioned using a time step scaling based on the chemical production source terms in the species equations. The sharp corner at the projectile base was treated as a grid cut-out region using a single non-rectangular computational domain. A more complete description of the solution technique is given by Briley and McDonald (1977, 1980).

The approach used by Eklund, Drummond and Hassan (1990) was to treat the chemical source terms implicitly on a pointwise basis. Since an explicit solution procedure was used by Eklund, Drummond and Hassan (1990), this amounts to rescaling the time step in each individual species equation, and therefore allows each equation to relax at its own time scale. In this approach the species equations are still solved in an uncoupled manner at each time step.

The present fully implicit approach automatically includes the pointwise implicit coupling of the chemical source terms, and the coupling among the various species equations being solved. The CMINT code allows for the user specified coupling of the species equations, and coupling to the Navier-Stokes equations is optional as well. Therefore, if certain species do not contribute significantly to the energy balance, those equations could be solved decoupled from the other species and flow equations at each time step. This approach can save computer time per time step although the convergence rate may be adversely affected.

The coupling of the species equations involved in energetic reactions is important and improves overall convergence. However, the possibility exists that the species equation source terms will cause ill-conditioned matrices due to large off-diagonal

elements in the block matrix at a particular grid point. Obviously, this problem is not encountered when the species equations are solved one at a time (the decoupled approach). In order to solve this difficulty with ill-conditioned block matrices, a time step scaling was devised for the coupled species equations. This scaling factor was applied in addition to the spatial time step conditioning, which is applied to all equations.

The system of P.D.E.'s may be written as

$$\frac{\partial \mathbf{H}(\vec{\phi})}{\partial t} = \underline{\underline{D}}\,\vec{\phi} + \mathbf{S}(\vec{\phi}) \tag{45}$$

where $\underline{\underline{D}}$ is the nonlinear spatial difference operator matrix and $S(\vec{\phi})$ is the source term vector. The linearized difference equations are written as

$$\underline{\underline{A}}\,\frac{\Delta\vec{\phi}}{\Delta t} = \underline{\underline{\mathcal{L}}}\Delta\vec{\phi} + \frac{\partial \mathbf{S}}{\partial\vec{\phi}}\,\Delta\vec{\phi} + \underline{\underline{D}}\vec{\phi}^{\,n} + \mathbf{S}(\vec{\phi}^{\,n}) \tag{46}$$

where

$$\Delta\vec{\phi} = \vec{\phi}^{\,n+1} - \vec{\phi}^{\,n} \tag{47}$$

and

$$\underline{\underline{A}} = \frac{\partial \mathbf{H}}{\partial\vec{\phi}} \quad , \quad \underline{\underline{\mathcal{L}}} = \frac{\partial \underline{\underline{D}}}{\partial\vec{\phi}} \tag{48}$$

The species equation source terms would appear as $S(\vec{\phi})$ terms and these terms can cause ill-conditioned matrices due to the form of the chemical production terms in Eq. (17).

The conditioning factor for the coupled species equations is chosen to insure diagonal dominance of the block matrix. First, the maximum absolute value of the operator $\partial S/\partial\vec{\phi}$ off-diagonal elements is determined at each grid point for each of the coupled species equations. Then the time derivative matrix $\underline{\underline{A}}$ is replaced by

$$\tilde{A}_{ij} = F_i A_{ij} \tag{49}$$

for the i^{th} coupled species equation. The factor F_i is given by

$$F_i = \max\left[1.0, \frac{C_s \max\left|\frac{\partial S_i}{\partial \phi_j}\right|_{j \neq i}}{A_{ii}/\Delta t}\right] \tag{50}$$

where the constant C_s is an arbitrary parameter with values of 0.1 and 1.0 used in the present applications. This amounts to rescaling the time step operators for ρ and Y_i in each of the coupled species equations. Note that this scaling is neither defined nor used for a decoupled species equation.

2.6 Two-Phase Flow Analysis. Two-phase flow effects may be present in certain projectile base burn applications depending primarily on the propellant formulation, particle size distribution, and burning rate. The M864 base burn projectile uses an ammonium perchlorate (AP) oxidizer based fuel, and generally is expected to generate mostly gaseous combustion products upon exiting the projectile base. Some small AP particulates ($\approx 5\ \mu$m or less) may remain in the injected gas. Therefore, a sophisticated two-phase flow analysis for projectile base flow applications is probably not required. An existing two-phase flow code (Sabnis, Gibeling and McDonald 1987) was adapted to the projectile application and tested on a representative base combustion problem.

Computational techniques used in simulation of two-phase flows can be broadly categorized into two approaches, viz. the Eulerian-Eulerian analysis and the Eulerian-Lagrangian analysis. Both techniques involve computing the continuous phase using an Eulerian analysis. The influence of the discrete phase (either solid particles or liquid droplets) on the continuous phase is accounted for by inclusion of inter-phase coupling terms in the Eulerian equations, which in the absence of these terms would be the usual Navier-Stokes equations. The discrete phase, on the other hand, may be treated with either a continuum model or a discrete model. The Eulerian-Eulerian technique uses a continuum model for the discrete phase and is commonly termed the two-fluid model. This approach models a dense granular bed very conveniently and this undoubtedly accounts for its popularity in modeling gun interior ballistics where large particle loading ratios occur over most of the cycle (e.g., Gough 1977 and Gibeling, McDonald and Banks 1983). The Eulerian-Lagrangian approach employs a Lagrangian description to analyze the motion of the discrete phase, using computational "particles" to represent a collection of physical particles. Newton's law of motion is employed to simulate the particle motion under the influence of the local environment produced by

the continuous phase. The discrete phase attributes (such as the particle position and velocity vectors, size, temperature, etc.) are updated along the trajectories.

In simulation of flows containing burning particles or evaporating droplets, it becomes necessary to account for the fact that the discrete phase is not mono-dispersed. To accomplish this in the Eulerian-Eulerian methodology, the two-fluid model can be generalized into a multi-fluid model. However, the CPU time requirements increase rapidly with increasing number of particle size classes, since an extra "fluid" has to be added for every particle size class, thereby increasing the number of partial differential equations. The Eulerian-Lagrangian analysis, on the other hand, treats the particle size as one of the attributes assigned to computational particles and hence has no trouble simulating flows which involve changing particle size. Since this approach involves integration of ODE's for the particulate phase, it is numerically efficient. Furthermore, the deterministic nature of the particle dynamics facilitates the incorporation of models for turbulent dispersion, agglomeration, collision, etc.

In Eulerian-Lagrangian algorithms, the inter-phase coupling terms for the continuous phase equations can be computed using a particle trajectory approach or a particle distribution approach. In the particle trajectory approach, the coupling terms are computed from the knowledge of the trajectories for representative particles and their attributes at the intersection of the trajectories with the Eulerian cell boundaries. In the particle distribution approach, the coupling terms are computed from the instantaneous distribution of the particles in the computational domain. The trajectory approach has been employed, for example, by Crowe, Sharma and Stock (1977), and Gosman and Ioannides (1983), while the particle distribution approach has been utilized by Dukowicz (1980) and Sabnis, Gibeling and McDonald (1987).

In the algorithms based on the trajectory approach, the integration of the Lagrangian equation of motion for representative particles is carried out starting from the injection location until the particle leaves the computational domain or until its size becomes negligible. During this interaction, the continuous phase flow field is held frozen. The inter-phase coupling terms for the continuous phase conservation equations are computed for every Eulerian cell from the net influx of the appropriate conserved variable into the Eulerian cell, due to all trajectories intersecting the particular Eulerian cell. The coupling terms thus computed are used to calculate the continuous phase flow field which can then be used to re-evaluate the trajectories and the source terms. This iterative process is continued until the desired level of convergence is achieved. These algorithms are thus inherently unsuitable for transient calculations and, further, the global iteration procedure used can require substantial computer time.

In the particle distribution approach, such as that used by Dukowicz (1980) and Sabnis, Gibeling and McDonald (1987), the source terms are computed from the instantaneous interaction between the continuous phase and all the particles in the particular Eulerian cell. Thus, the source term for the continuous phase continuity equation, for example, is given by the sum of the mass transfer rates for all the particles in the cell. The calculation procedure consists of updating the particle distribution through one time step followed by updating the continuous phase flow field through one time step. In general, it is not necessary that the time step used to integrate the particle motion and that used in updating the continuous phase flow field be equal. However, by making the two time steps equal, the particle distribution algorithms can be used for simulation of transient phenomena. If only a steady-state solution is desired, then the two time steps can be made unequal and matrix preconditioning techniques can be used for convergence acceleration of the continuous phase solution.

The present analysis is based on the CELMINT (Combined Eulerian Lagrangian Multidimensional Implicit Navier-Stokes Time-dependent) code developed by Sabnis, Gibeling and McDonald (1987). In this algorithm, the ensemble-averaged Navier-Stokes equations (including the inter-phase coupling terms) are solved for the continuous phase. A particle distribution model is used in the Lagrangian treatment of the particulate phase. The key feature of the particle transport model in CELMINT is that it integrates the Lagrangian equations of motion for a particle in computational space rather than physical space. This simplifies the computation of the interphase coupling terms, because the search for the mesh cell location of a particle becomes trivial.

The CELMINT code has been validated previously (cf. Sabnis et al. 1988) using the experimental data reported by Milojevic, Borner and Durst (1986) for two-phase shear-layer flow without inter-phase mass transfer. More recently (cf. Sabnis and de Jong 1990), this Eulerian-Lagrangian analysis was utilized to simulate the two-phase flow in an evaporating spray and the calculated results were compared with the experimental data of Solomon et al. (1984). The equations to be solved for the continuous phase are the mass, momentum, and energy conservation equations including the appropriate source terms to account for the influence of the particulate phase on the continuous phase. The form of these terms for a single species particle is given in Sabnis, Gibeling and McDonald (1987) and Sabnis and de Jong (1990).

Under the present effort the Lagrangian module was modified for application to projectile base combustion with particles using the CMINT code. This module could be implemented in other Navier-Stokes codes if desired. For the base flow problem a boundary definition routine is required to permit calculation of particle motion with

realistic boundary interactions. A restitution coefficient model is used for particle-wall collisions (de Jong, Sabnis and McConnaughey 1989). The present application has been tailored for the analysis of ammonium perchlorate (AP) vaporization, since these are the most likely particles to be emitted from the projectile base burning propellant. The equilibrium products for the self-deflagration of AP are O_2, N_2, H_2O and HCl; it is reasonable to replace the HCl with an equivalent amount of CO and N_2. Therefore, the particulate AP is assumed to consist of the following species in the present analysis.

Species	Mass Fraction (f_i)	Molecular Weight
O_2	0.368	31.999
N_2	0.354	28.013
H_2O	0.253	18.015
CO	0.025	28.01
Mixture:	1.000	25.58

A vaporization model based on a Sherwood number analysis for an isolated spherical particle has been incorporated into the Lagrangian calculation procedure. A linear regression burning rate has been used in the analysis, and the burning rate has been obtained from the available AP strand burning experimental data for the M864 propellant. The resulting rate of gas mass production of species i due to particle burning under these assumptions may be written as,

$$m_i = \dot{m}_v \, f_i \tag{51}$$

where f_i is the AP species mass fraction from the above table. The particle vaporization rate is assumed to enhanced by gas convection around the particle, and is given by,

$$\dot{m}_v = -0.5 \, Sh \left[4\pi \, R_p^2 \, \rho_p\right] R_{p,t} \tag{52}$$

The rate of change of particle radius, $R_{p,t}$, is a negative constant for linear regression, and the Sherwood number, Sh, is the mass transfer analogy of the Nusselt number for heat transfer. The Sherwood number is assumed to be the same as the Nusselt number for an isolated spherical particle, which is based on the relative velocity between the gas

and particle, i.e.,

$$Sh = 2 + 0.53\ (Re_p)^{0.5} \quad \text{for } Re_p < 278.92$$
$$Sh = 0.37\ (Re_p)^{0.6} \quad \text{for } Re_p \geq 278.92 \tag{53}$$

where the particle Reynold's number is defined as,

$$Re_p = \frac{\rho\ 2R_p\ |\vec{U} - \vec{U}_p|}{\mu} \tag{54}$$

Complete details of the combined Eulerian-Lagrangian procedure using the CMINT code are given in Sabnis, Gibeling and McDonald (1987), Sabnis et al. (1988), and Sabnis and de Jong (1990) and are not repeated here. A sample calculation has been performed and is discussed in the section on Base Flow Applications.

3. REACTING FLOW VALIDATION CASE

A supersonic flow coaxial burner (SSB) studied experimentally by Jarrett et al. (1988) has been selected as a validation case for the present analysis. While this case only considers H_2 combustion, it is well documented and a digital version of the data is available from Jarrett et al. (1988). Also, this case has been analyzed numerically by Jarrett et al. (1988) and Eklund, Drummond and Hassan (1990). A schematic of the SSB apparatus and computational domain is shown Fig. 1. The SSB consists of an inner hydrogen jet exiting at M = 1.0 with a coaxial vitiated air jet exiting at M = 2.0. The inflow boundary conditions for the calculations, based on the ideal burner exit conditions obtained from Jarrett et al. (1988), are given in Table III. The SSB nozzle walls are conical with a half-angle of 4.3 degrees. The fuel injector is a cone-cylinder geometry as shown in Fig. 1, and a shock wave emanating from the cone-cylinder juncture leads to some uncertainty in the jet conditions specified in Table III, as noted by Eklund, Drummond and Hassan (1990). The Eggers turbulence model as modified by Eklund, Drummond and Hassan (1990) was used for this case (see section 2.4.4).

Three different Cartesian grid systems have been used on this case to determine the effect of mesh refinement on the solution. The first grid utilized 101 radial points and 61 axial points; the second used 101 radial and 101 axial points (Fig. 2); and the third used 111 radial and 121 axial points. All grids used nonuniform distributions in both

directions. It can be seen that the lip between the fuel injector and coaxial air stream is well resolved in the second grid, while the outer nozzle lip has poorer resolution. The third grid was constructed based on the solution using the second grid to better resolve regions of steep gradients.

Calculations were first made on the three grids using a nine reaction set consisting of reactions one through nine from Table II. A final calculation was made on the third grid by deleting the ninth reaction to determine its importance in this case, which was not significant. All of the calculations were started by assuming the unmixed jets extended to the outflow boundary with a blending region between the fuel and air streams. The initial constant pressure throughout was set equal to the pressure of the vitiated air stream. The pressures at the hydrogen exit and all ambient boundaries were modified over 100 iterations (time steps) to achieve the values specified in Table III.

The results of the calculation on the second grid (101 $\times$ 101) are shown in Figs. 3 through 6, and the temperature prediction on the first grid (101 $\times$ 61) is shown in Fig. 7. The computed solution using the third grid is very close to that in Figs. 3 through 6, hence those results are omitted here. The results shown are for axial stations at 25.4 mm (one inch) intervals starting at the nozzle exit. The inflow axial velocity shown in Fig. 3a indicates a significant difference in the starting values used in the CFD simulations versus the experimental results. This may be caused by experimental error due to seed particle "lagging" in the high shear regions or to distortion of the actual velocity profile due to the nozzle and fuel injector configuration. Also, as noted by Jarrett et al. (1988) the CARS and LDV measuring volumes are not small compared to the fuel injector diameter, which will result in flattened experimental profiles in regions of large gradients.

The velocity profiles and O_2 and N_2 number density profiles were not significantly different as a result of the grid refinement, hence those figures for the first grid have been omitted here. The computed axial velocities are seen to lead the experimental values slightly at all measuring stations, and to a lesser extent in the results of Jarrett et al. (1988). Eklund, Drummond and Hassan (1990) did not show velocity predictions. It should be noted that the LDV turbulence measurements Jarrett et al. (1988) show large anisotropic turbulent stresses which are not modeled by simple algebraic turbulence models employed in the various calculations. Since much of the initial flow field change is shear driven, the use of an isotropic model should result in some differences between computation and experiment.

The temperature comparison with data is shown in Figs. 4 and 7, where it is seen that the present results underpredict the core region temperature at an axial location

$x = 25.4$ mm, while over predicting the temperature somewhat at $x = 76.2$ mm. The results on the finer grid (Fig. 4) agree very well with the data elsewhere. The calculation of Jarrett et al. (1988) shows a similar discrepancy in temperature at $x = 25.4$ mm and a slight overprediction at $x = 101.6$ mm, and shows close agreement at the other two stations. Eklund, Drummond and Hassan (1990) underpredicted the temperature in the core at all stations except $x = 50.8$ mm where their results are very close to the data.

The data at $x = 25.4$ mm possibly indicates that fuel ignition has taken place sooner than predicted, which is the opposite of what is expected. In a recent private communication, Jarrett (1991) indicated the discovery of a systematic error in the data reported in Jarrett et al. (1988). Also, the availability of more recent measurements on the same apparatus Cheng et al. (1991) was noted. The data of Cheng et al. (1991) is not yet available in digital form; however, the figures in Cheng et al. (1991) show that the fuel has not ignited at 25.4 mm, and in fact the present temperature prediction at that location is closer to this new data.

The present predictions show somewhat larger differences in O_2 number density (Fig. 5) than either Jarrett et al. (1988) or Eklund, Drummond and Hassan (1990), while the N_2 number density is much closer to the data. The spreading rate evident from Figs. 5 and 6 is somewhat larger than that obtained by either Jarrett et al. (1988) or Eklund, Drummond and Hassan (1990). In general, the level of agreement between the present predictions and experiment is quite good considering the uncertainties and approximations involved.

This validation case provides a level of confidence in the finite rate chemistry model implementation in the present code. Also, the reaction set utilized in this case is a subset of the H_2-CO reaction set used in the base combustion calculations, and this case implies a limited validation of the reaction set and rate constants employed.

4. PROJECTILE APPLICATIONS

4.1 Boundary Conditions. Since only supersonic flow ($M_\infty = 2$) was considered in the present base flow calculations, the upstream boundary conditions were obtained from a full projectile calculation (Nietubicz and Heavey 1990). Specified values for all the dependent variables were set on this boundary. For the full projectile calculations, specified values were set for the dependent variables on the freestream boundary ahead of the projectile. On the outer radial boundary specified supersonic conditions were set from the upstream boundary to the axial station of the projectile base, and downstream

of this station extrapolation was used. The outer boundary was located sufficiently far from the projectile so that waves emanating from the body pass through the downstream boundary. At the projectile surface no-slip conditions, a specified wall temperature ($T_w = T_\infty = 294$ K), zero normal pressure gradient and zero gradient of species mass fractions were specified. Along the base injection region stagnation temperature, axial mass flux and species mass fractions were specified, while the pressure was determined from the normal momentum equation and the radial velocity component was assumed to be zero. At the downstream supersonic outflow boundary, first derivative extrapolation was used.

4.2 Flat Base Projectile Case. The M864 projectile with a flat nose and a flat base was considered to obtain a forebody flow field solution as a starting condition for the supersonic base flow computation. The projectile schematic is reproduced in Fig. 8 from Danberg (1990). An algebraic grid was generated for this configuration with clustering near the nose and the projectile surface (Fig. 9). The resolution downstream of the base was sacrificed since only the forebody solution was required from this calculation. In fact, the results shown were obtained by assuming an extended sting downstream of the base. In this case the axial direction grid line emanating from the projectile base corner was assumed to be a solid surface, and points between the centerline and this surface were excluded from the calculation. The grid consisted of 100 radial points and 280 axial points with 28 points between the centerline and the projectile nose corner, 65 axial points upstream of the nose, and 250 axial points from the inflow boundary to the end of the projectile.

The calculation was run assuming that $T_{wall} = T_\infty = 294$ K, $M_\infty = 2.0$, and a freestream pressure of 100,000 Pascals. A time step conditioning scheme (i.e., spatially varying time step) was utilized successfully to obtain good convergence throughout the flow field. The surface pressure distribution for this case is shown in Figure 10, where the projectile nose is located at X/D = 0.1197. The present results indicate a stagnation pressure on the nose of $p_n/p_\infty = 5.89$, with a rapid drop in pressure around the sharp corner. An overexpansion to a normalized pressure of 0.34 is observed, followed by a rapid recovery to the expected level. Comparison of the present results with those of BRL show the two calculations to be virtually identical beginning slightly downstream of the flat nose except for a slight axial shift, as shown in Fig. 10.

5.0 BASE FLOW APPLICATIONS

5.1 Non-Reacting Flow Cases. Under the present study the initial base flow calculations were performed with an algebraically generated grid. A grid consisting of 130 radial by 230 axial mesh points was constructed for the base flow calculation. The upstream boundary for this grid was placed at X/D = 4.35 which is about one caliber upstream of the start of the boattail. There were 58 grid points between the centerline and the projectile base corner. The grid was refined in the axial direction adjacent to the base with 160 points between the base and the downstream boundary located approximately 4.2 calibers from the projectile base. Initial conditions for the base flow calculations were obtained from the previously discussed forebody solution. The base flow calculation was started using a simple mixing length model and run for 100 time steps to allow the base flow to develop. Then the calculation was restarted using the Jones and Launder (1972) low Reynolds number form of the k-ϵ turbulence model.

The calculation was run to convergence with a reduced artificial dissipation coefficient everywhere except near the projectile base corner. A drag coefficient $C_{DB} = 0.149$ was obtained. The base pressure distribution for this case, shown in Fig. 11, is relatively flat; however, the turbulent viscosities predicted very near the projectile base were unrealistically large. This may be due to inadequate axial grid resolution near the projectile base, since the Jones-Launder k-ϵ formulation is sensitive to near wall grid spacing. Figure 11 also shows the prediction with the BRL axisymmetric code and a mixing length turbulence model (Baldwin-Lomax/Chow), and a second k-ϵ model result using the BRL grid for the base region (139 x 166). This grid has an axial spacing at the base ($\Delta x_B/D$) of 0.0015 which is about 100 times larger than the spacing in the 130 x 230 grid. The latter grid shows some pressure oscillations near the corner, but otherwise only a moderate difference from the more refined 130 x 230 grid. As discussed in the following subsection, 5.2, when a mixing length model was used with the present analysis, results which are very similar to the BRL results were obtained.

A dome base M864 projectile configuration was also considered for the nonreacting cases considered. A base region grid consisting of 150 radial and 230 axial points was constructed using the EAGLE code (Thompson 1987). The upstream boundary for this grid was placed at X/D = 4.35, and the flow conditions were the same as in the flat base case. The base flow calculation was run with the k-ϵ model and a reduced artificial dissipation coefficient except in the immediate base region. The drag coefficient obtained was $C_{DB} = 0.147$. It should be noted that the results achieved with the CMINT code showed sensitivity to the grid resolution and the second order artificial

dissipation coefficient when the k-ϵ model was employed.

A further correction to the k-ϵ model was implemented to ascertain the influence on base drag. The high Mach number modifications suggested by Childs and Caruso (1987) lead to a base drag coefficient of $C_{DB} = 0.133$ for the dome base case. The streamline curvature modification suggested by Childs and Caruso (1989) was not successfully employed in the dome base case. However, the results of Childs and Caruso indicated that the streamline curvature modifications tended to offset the high Mach number corrections for the case they considered. No additional consideration of turbulence model related issues was carried out under this effort.

5.2 Hot Injection and Reacting Flow Cases. Subsequent calculations under this project were carried out for a flat base M864 projectile with a three degree boattail angle using a full grid provided by BRL. The flat base case was selected for the remaining calculations to reduce geometry related complications in the combustion model development. This grid has 70 radial points from the centerline to the projectile base corner and 120 axial points from the base to the outflow boundary. A modified grid for the base region only was constructed using this grid. The reacting flow calculations required more grid points in both the radial and axial directions than either nonreacting or air injection cases. The grid utilized for the base calculations has 100 points radially from the centerline to the base corner, and 69 points from the corner to the outer boundary. There are 30 points in the injection region which extends from the centerline to a radius of 0.16 caliber. In the axial direction there are 46 points upstream of the base, and 150 points from the base to the outflow boundary. The computational grid used in the base flow calculations is shown in Fig. 12. The near-wall grid resolution in the transverse direction (i.e., $\Delta r/D$) was 2×10^{-5}, which provides sublayer resolution. In the axial direction, the spacing at the projectile base (i.e., $\Delta x_B/D$) was 2×10^{-4}, where D is the maximum projectile diameter. This axial spacing is about 7.5 times smaller than that in the original BRL grid.

Calculations were performed for the M864 flat base projectile for the following four cases: (a) without base injection, (b) with hot air injection, (c) with H_2 injection and (d) with H_2-CO injection. Case (c) used the global reaction model of Rogers and Chinitz (1983), while case (d) used the finite rate model consisting of reactions 1 to 8 and 10 to 12 in Table II. For case (d) the injectant species mass fraction are shown in Table I, while for case (c) the mass fraction of H_2 was selected to give the same fuel heat of combustion. The diluent species in the injectant was H_2O. Also, the molecular weight of the injected H_2 was artificially increased to yield the correct fuel molecular weight.

Figure 13 shows the favorable comparison between the SRA and BRL base pressure distributions without base injection. The differences between the grid distributions for the two calculations were noted above, and is expected to account for some of the observed minor differences in base pressure.

The number of iterations required for convergence of the reacting base flow calculations was about 5500, which was much larger than that needed for the Jarrett validation case. This is due to the complicated recirculation and mixing patterns which occur in the base flow region. Also, grid resolution in the shear layers and reaction zone will influence the convergence rate, and no attempt was made to optimize the grid for the present cases. All cases with injection presented here have an injection parameter, I = 0.0022, where

$$I = \frac{m_i}{\rho_\infty U_\infty A_{base}} \tag{55}$$

and m_i is the injection mass flow rate. This is a typical value for I at projectile launch Danberg (1990). The stagnation temperature of the injected gas in both cases (b) and (d) was 1533 K, while for case (c) it was 1755 K. Although the higher injection temperature for case (c) will have a direct impact on the base drag coefficient, the qualitative features of the flow are representative. The molecular and turbulent Schmidt numbers for case (c) were both 1.0, while for case (d) they were 0.7 and 1.0, respectively. Reduction of the molecular Schmidt number for case (c) was not carried out; however, based on calculations for H_2-CO injection, the drag coefficient is expected to decrease slightly (about 7 percent). In reality, the molecular diffusion of a hydrogen-air mixture is not correctly represented by Fick's law and the Schmidt number approximation. In a turbulent flow the errors encountered tend to be small since the molecular mixing is often much less than the turbulent mixing. In the present case, the effect of the Schmidt number change is not totally negligible; however, a greater concern is the turbulence prediction in the base region since the mixing of reactants clearly will have an important influence on the combustion process and the resulting base drag.

The base drag coefficient, C_{DB}, is defined in terms of the maximum projectile diameter D and the average base pressure P_B as

$$C_{DB} = \frac{\int_{base} [P_\infty - P]\, dA}{\frac{1}{2}\rho_\infty U_\infty^2 A_D} \; ; \qquad A_D = \pi D^2/4 \tag{56}$$

The present calculations yielded values of C_{DB} for cases (a),(b), (c), and (d) of 0.167, 0.138, 0.118 and 0.089, respectively. Clearly, there is significant reduction in the base drag as a result of hot air injection and combustion. The results shown here are consistent with the predictions of Nietubicz and Sahu (1988) with both no injection (C_{DB} = 0.167) and hot air injection (C_{DB} = 0.136). With the ninth reaction included in the calculation the drag coefficient obtained with H_2-CO combustion was also about 0.089, which indicates the relative unimportance of that reaction in the present application. The base pressure distributions for these four cases are compared in Fig. 14. A considerable flattening of the base pressure distribution is evident as a result of both hot gas injection and combustion.

Temperature contours and velocity vectors for the four cases are presented in Figs. 15 (a,b,c,d) and 16 (a,b,c,d), respectively. From Figures 15 and 16 it can be seen that the effect of hot air injection is confined to the region very close to the base. The H_2 combustion case (c) shows a larger effect, while the H_2-CO combustion case (d) shows a much more extensive region of influence. In addition, the stand-off distance of the recirculation region increases only slightly in the combustion cases (c) and (d). The effect on the base pressure may be explained as follows. The injection of gas into the base region will move the recirculation downstream even with cold injectant. This process will result in a downstream shift in the wake closure location (the viscous throat) and a somewhat reduced expansion at the base corner, which implies an increase in base pressure.

With hot air injection the temperature increases throughout the base region as seen by comparing Figs. 16a and 16b, and there is a resulting decrease in Mach number. Hence a longer distance downstream is required for the flow to reaccelerate to M = 1 and the viscous throat moves further downstream, which implies a weaker corner expansion and higher base pressure. Strahle, Hubbartt and Walterick (1982) explained this behavior in terms of the temperature increase (Mach number decrease) along the stagnation streamline.

In the combustion cases the wake region becomes hotter than with hot air injection. The rear stagnation point moves even further downstream and the corner expansion becomes even weaker, which results in an additional increase in base pressure. With H_2 combustion (case c) the flame zone is very close to the injection plane, and the temperatures reached are higher than with H_2-CO combustion (case d). In the latter case the region of combustion is more distributed, and temperatures are elevated over much more of the projectile wake region. The effect on the base corner expansion and the recompression region as a result of hot air injection and combustion is readily

observed by comparing the free stream temperature contour in each case. These are shown in Fig. 17 along with the rear stagnation point location for all cases.

5.3 Mesh Refinement Study for Reacting Flow. A number of axial grid refinement calculations were performed on the flat base case with combustion. This was done to assess the influence of axial mesh spacing in the base region reaction zone. The importance of the axial spacing at the projectile base and near the downstream stagnation point was also identified. The original case considered in the previous section (case d) had an axial spacing $\Delta x_B/D = 0.0002$ at the base. The subsequent grids used a relaxed spacing of $\Delta x_B/D = 0.0015$ at the base to permit the concentration of points in the reaction zone without using an excessive number of points. The latter spacing is the same as that in the original BRL grid, which has been used by BRL personnel in base flow calculations.

Table IV indicates the axial grid spacing in three relevant locations downstream of the base: (1) $\Delta x_B/D$ is the spacing at the projectile base, (2) $\Delta x_1/D$ is the spacing in the vicinity of the first stagnation point (closest to the base), and (3) $\Delta x_2/D$ is the spacing in the vicinity of the downstream stagnation point.

One conclusion which can be reached from these results is the importance of the axial spacing at the base upon the oscillatory nature of the base pressure convergence history. The drag coefficients reported in the oscillatory cases (g, h and i) are an average taken from the plot of C_{DB} versus time step number. With this in mind it appears that a reduced reaction zone spacing characterized by $\Delta x_1/D$ is not critical to the base drag value; however, it is possible that overall convergence would improve if $\Delta x_B/D$ was also reduced to the case (d) value. Also, the cases with too large a spacing in the downstream stagnation region ($\Delta x_2/D$) had significant convergence problems.

5.4 Two-Phase Reacting Flow Case. A sample two-phase flow calculation has been considered with injection of ammonium perchlorate (AP) from the projectile base. Actually, the particle injection was initiated slightly downstream of the gas injection location (at x/D = 5.925) to avoid transporting the particles through the Eulerian fine grid region adjacent to the base. The particle mass flux was assumed to be one per cent of the injection gas mass flux, and the initial particle diameter was 5.0 microns. The effect of the AP burning on the base combustion process is primarily to supply additional O_2 in the base region; however, the relatively low AP mass flux and the external freestream air supply implies that the effect on the base combustion process should be

small. This was observed in the calculation which was performed by restarting the converged gas (H_2/CO) combustion case and running an additional 100 time steps. Particles of diameter less than 1.0 micron were removed from the calculation. Figure 18 shows traces of representative particles injected as described above. These traces show a fairly slow burnout of the AP particles with the assumed linear regression rate. Note that the injection gas composition was not modified for the particle injection case. If a significant fraction of the propellant AP did not burn in the combustion chamber, then the equilibrium composition of the combustion products would have to be recalculated to provide new gas injection boundary conditions.

6. CONCLUDING REMARKS

Both global and detailed finite rate chemistry models have been incorporated into an existing Navier-Stokes computer code and the result has been applied to the problem of combustion in the base region behind a projectile in supersonic flight. Prior to considering base flow and combustion cases, the code was calibrated against a code run by Ballistic Research Laboratory and when similar grid and turbulence models were used, similar results were obtained. The reacting flow capability was validated through comparison with a documented H_2 supersonic flow coaxial burner experiment. When considering the effects of base injection/combustion, four cases were simulated. These were: (a) no injection, (b) hot air injection, (c) H_2 base combustion and (d) H_2/CO base combustion. The predicted base pressure increase (base drag decrease) is progressively larger with hot air injection, H_2 base combustion, and H_2-CO combustion. The detailed computations show the base pressure variation to be intimately related to the effect on the base corner expansion and the wake recompression region. With only H_2 injection higher flame temperatures are reached very near the projectile base and lower temperatures occur in the wake region. The inclusion of CO in the injected fuel retards the reaction process and lowers the peak temperature reached near the projectile base. However, the more distributed nature of the base combustion yields higher temperatures throughout the wake region than with H_2 alone. It appears reasonable to include both H_2 and CO in the analysis for the base region flow physics with combustion.

Preliminary base flow calculations employed the Jones and Launder low Reynolds number k-ϵ turbulence model, while subsequent calculations used the Baldwin-Lomax model on the projectile forebody and the Chow wake mixing model downstream of the projectile base. The k-ϵ model calculations showed a much flatter base pressure

distribution than the Chow model, although this may be a result of performing the k-ϵ simulation on a grid with which the axial resolution next to the base adequate for a mixing length approach but too coarse for a viable k-ϵ approach, indicating the need for considerably higher near base resolution if k-ϵ were to be used. Uncertainties in the base region turbulence model for nonreacting flows appear to have a second order effect on the base drag coefficient as shown by both present computations and those by BRL personnel. An axial mesh refinement study for the reacting base region flow demonstrated the importance of adequate axial resolution in the vicinity of the downstream stagnation (wake closure) point. Additional axial grid refinement in the combustion region over that in the baseline case did not significantly change the results or improve the convergence rate of the solution.

A validation calculation was performed for a coaxial hydrogen-air supersonic burner, and the comparison with the available experimental data was very good. This case demonstrates the validity of the H_2 reaction set which is a subset of the H_2-CO reaction set used in the projectile base combustion simulations. Direct validation of the base combustion models developed is not possible without additional experimental data for base combustion flows. Since such data is presently unavailable, the validity of the computed results can only be inferred from the comparison of base drag coefficients with those implied by transonic range data for an actual projectile firing.

Further work should be performed in the area of turbulence - combustion interaction to better understand the impact of turbulence unmixedness on the H_2-CO combustion process in the base region flow. Validation of any models would require a well documented base flow experiment with detailed flow field, temperature and species data. Although a significant experimental effort would be required, both mean and fluctuating quantities should be obtained for proper model validation.

Table I. M864 Propellant Equilibrium Species Concentrations (Major Species, T = 1533 K, p = 0.68 atm)

	CET86 results		Equivalent mixture	
Species i	mole fraction	M_{W_i}	mole fraction	mass fraction
CO	0.249	28.01	0.265	0.3402
CO_2	0.069	44.01	0.160	0.3228
HCl	0.136	36.46	0.0	0.0
H_2	0.261	2.016	0.261	0.0241
H_2O	0.197	18.015	0.197	0.1627
N_2	0.085	28.01	0.117	0.1502
Sum	0.997	(M_W) 21.81	1.000	1.000

Table II. Carbon Monoxide Oxidation Mechanism Including HO_2 and H_2O_2 Chemistry (Westbrook, et al. 1977 and Gardiner 1984)
Rate constant: $k_f = A\ T^b \exp(-E_a/R_uT)^+$

	Reaction	A	b	E_a (kJ/mole)	
1.	$H + O_2 = OH + O$	1.2×10^{17}	-0.91	69.1	Set B
2.	$H_2 + O = OH + H$	1.5×10^{7}	2.0	31.6	
3.	$O + H_2O = OH + OH$	1.5×10^{10}	1.14	72.2	
4.	$OH + H_2 = H_2O + H$	1.0×10^{8}	1.6	13.8	
5.	$O + H + M = OH + M$	1.0×10^{16}	0.0	0.0	
6.	$O + O + M = O_2 + M$	1.0×10^{17}	-1.0	0.0	
7.	$H + H + M = H_2 + M$	9.7×10^{16}	-0.6	0.0	
8.	$H_2O + M = H + OH + M$	1.6×10^{17}	0.0	478.0	
9.	$O_2 + H_2 = OH + OH$	7.94×10^{14}	0.0	187.0	
10.	$CO + OH = CO_2 + H$	4.4×10^{6}	1.5	-3.1	
11.	$CO + O + M = CO_2 + M$	5.3×10^{13}	0.0	-19.0	
12.	$CO + O_2 = CO_2 + O$	2.5×10^{12}	0.0	200.0	
13.	$H + O_2 + M = HO_2 + M$	2.0×10^{18}	-0.8	0.0	Set A
14.	$O + OH + M = HO_2 + M$	1.0×10^{17}	0.0	0.0	
15.	$HO_2 + O = O_2 + OH$	2.0×10^{13}	0.0	0.0	
16.	$H + HO_2 = OH + OH$	1.5×10^{14}	0.0	4.2	
17.	$H + HO_2 = H_2 + O_2$	2.5×10^{13}	0.0	2.9	
18.	$OH + HO_2 = H_2O + O_2$	2.0×10^{13}	0.0	0.0	
19.	$HO_2 + HO_2 = H_2O_2 + O_2$	2.0×10^{12}	0.0	0.0	
20.	$H_2O_2 + M = OH + OH + M$	1.2×10^{17}	0.0	190.0	
21.	$H + H_2O_2 = HO_2 + H_2$	1.7×10^{12}	0.0	15.7	
22.	$CO + HO_2 = CO_2 + OH$	1.5×10^{14}	0.0	98.7	
23.	$H_2O_2 + OH = H_2O + HO_2$	7.0×10^{12}	0.0	6.0	

+ Dimensions of k_f are $[cm^3/mole]^{(m-1)}$ where m is the reaction order; T is in Kelvin. Reverse rate constants k_b are obtained from k_f and the equilibrium constant K_c.

Table III. Exit Conditions for Jarrett SSB Coaxial Streams (Jarrett, et al. 1988)

	Hydrogen Jet	Vitiated Air Jet	Ambient Air
Mach number	1.0	2.0	0.0
Temperature, K	545	1180	300
Velocity, m/s	1772	1390	0.0
Pressure, MPa	0.112	0.107	0.101
Mass Fractions			
$Y(H_2)$	1.0	0.0	0.0
$Y(O_2)$	0.0	0.254	0.232
$Y(N_2)$	0.0	0.572	0.768
$Y(H_2O)$	0.0	0.174	0.0

Table IV. Summary of Computed Results for Projectile Base Combustion

Case	Axial Points	$\Delta x_B/D$	$\Delta x_1/D$	$\Delta x_2/D$	C_{DB} and Comments
d	196	0.0002	0.0136	0.02	0.089; Nearly monotonic convergence; 5500 steps.
e	176	0.0015	0.007	0.10	——— Slow convergence.
f	186	0.0015	0.003	0.18	——— Divergent.
g	186	0.0015	0.003	0.19	0.092 Erratic oscillatory convergence; 6000^+ steps.
h	186	0.0015	0.003	0.05	0.085 Oscillatory convergence; 6000^+ steps.
i	196	0.0015	0.0035	0.025	0.092 Oscillatory convergence; 7000^+ steps.

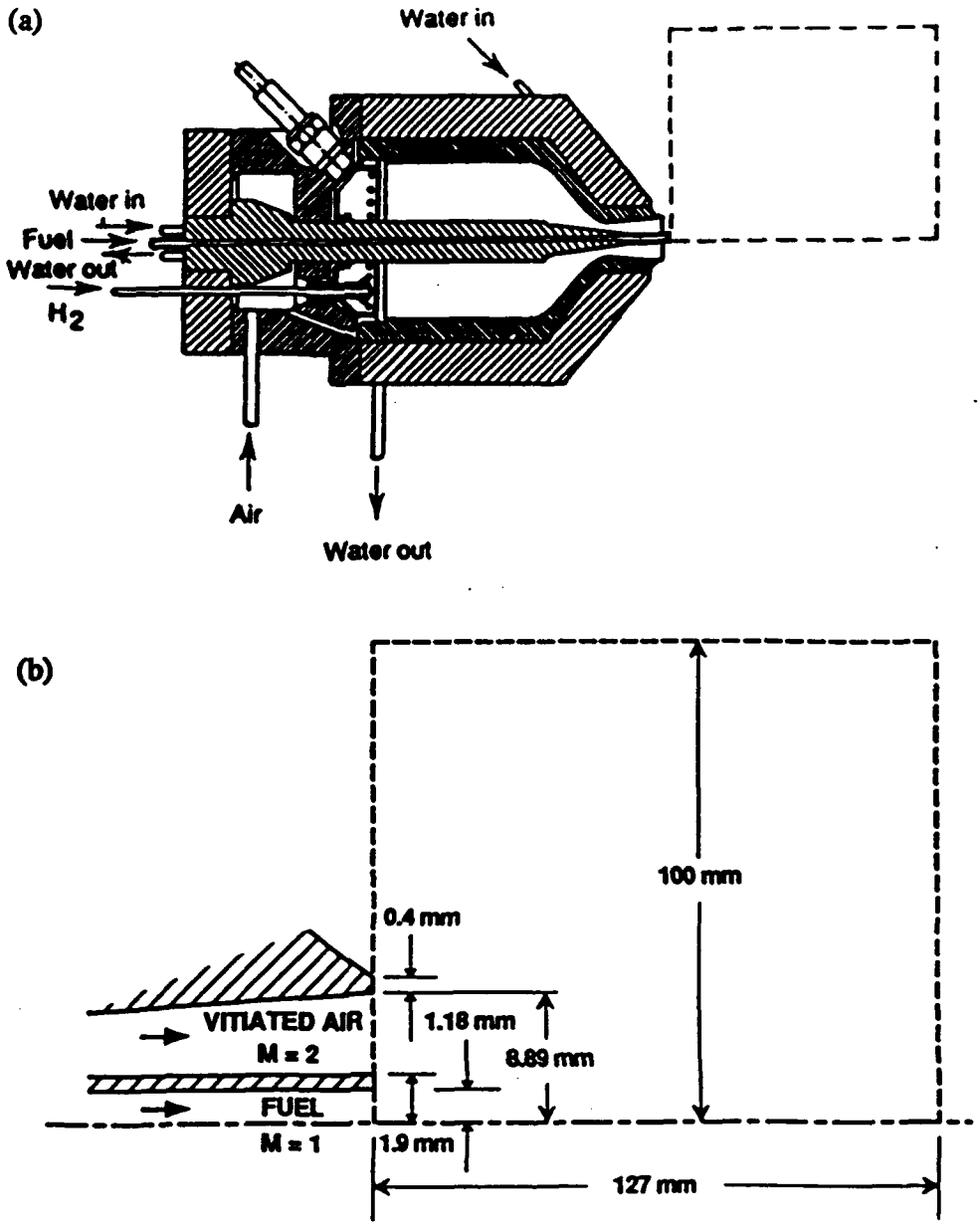

Figure 1. Jarrett SSB Experiment (a) Schematic of the Apparatus; (b) Computational Domain.

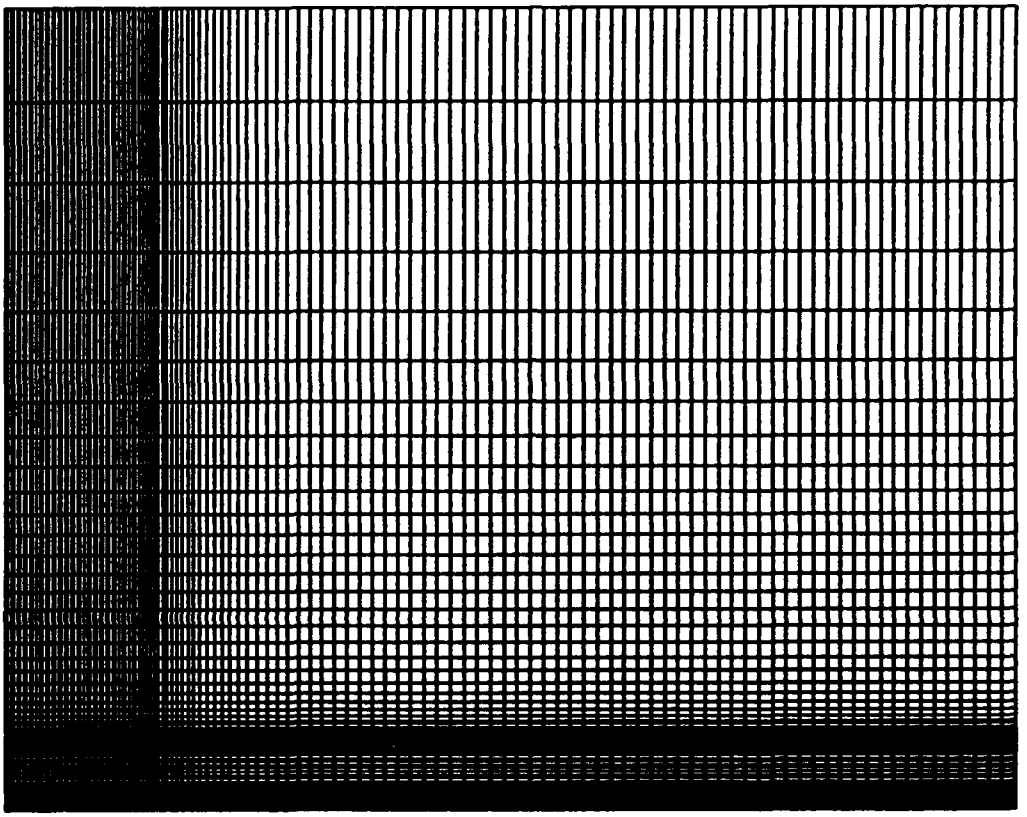

Figure 2. 101 x 101 Grid for Jarrett Supersonic Coaxial Burner Simulation.

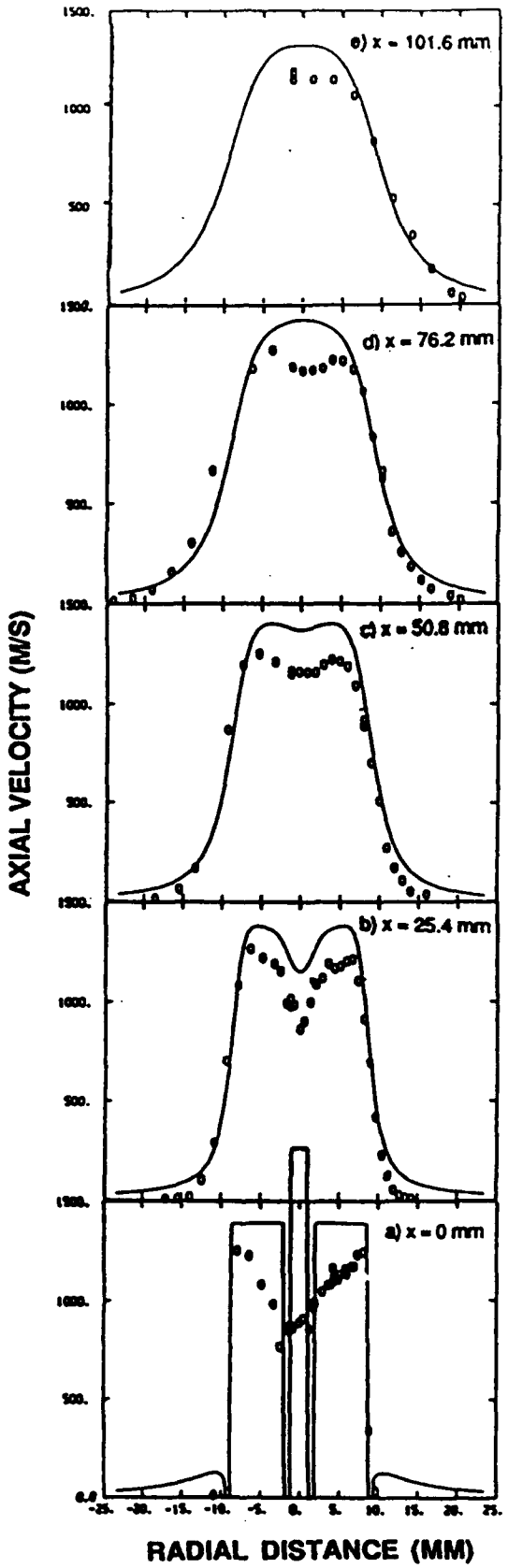

Figure 3. Jarrett SSB Simulation - Axial Velocity, 101 x 101 Grid.

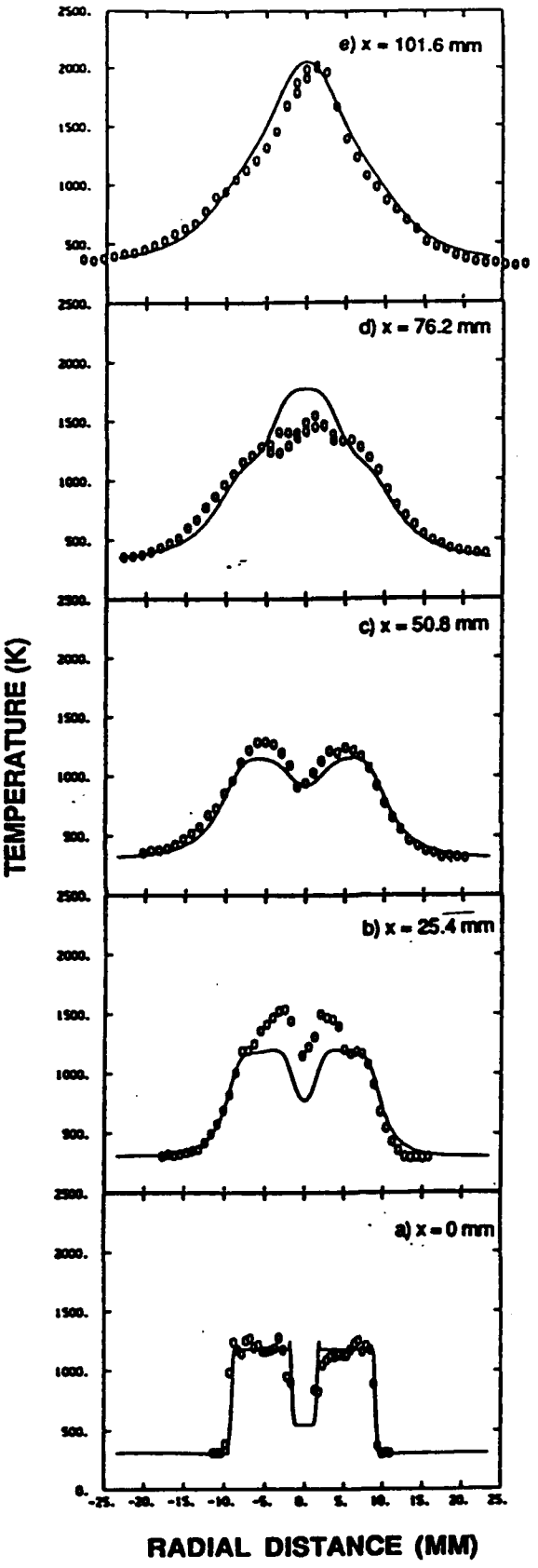

Figure 4. Jarrett SSB Simulation - Temperature, 101 x 101 Grid.

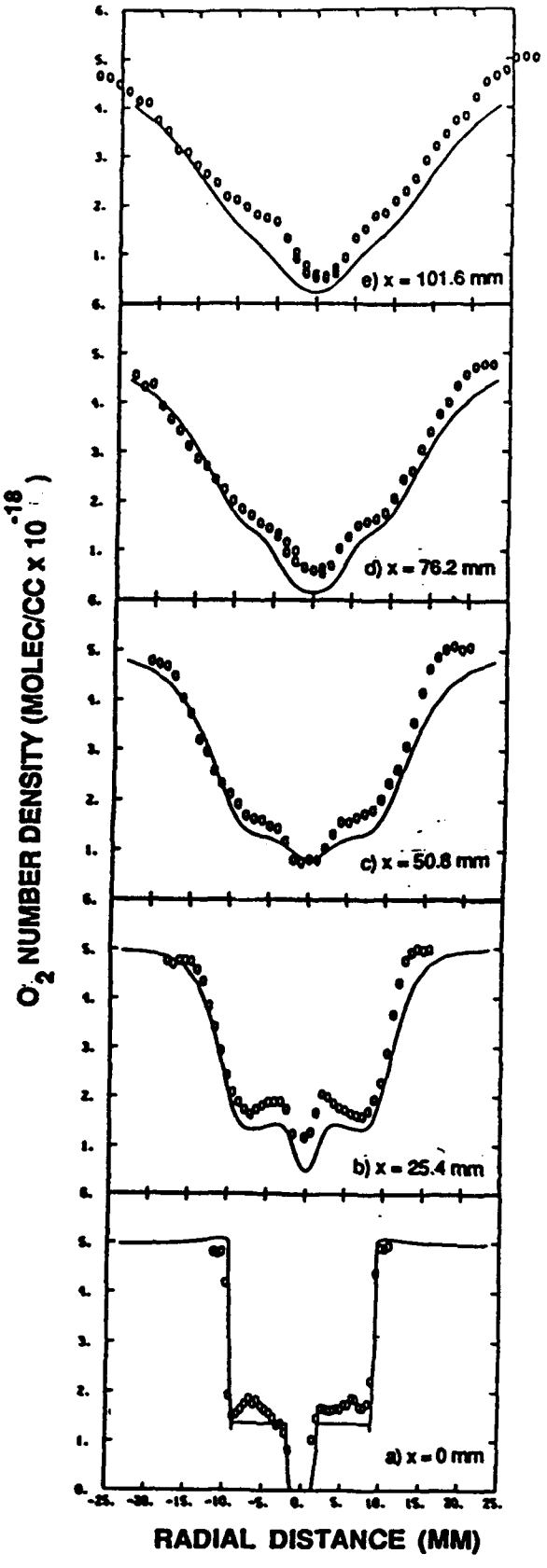

Figure 5. Jarrett SSB Simulation - O_2 Number Density, 101 x 101 Grid.

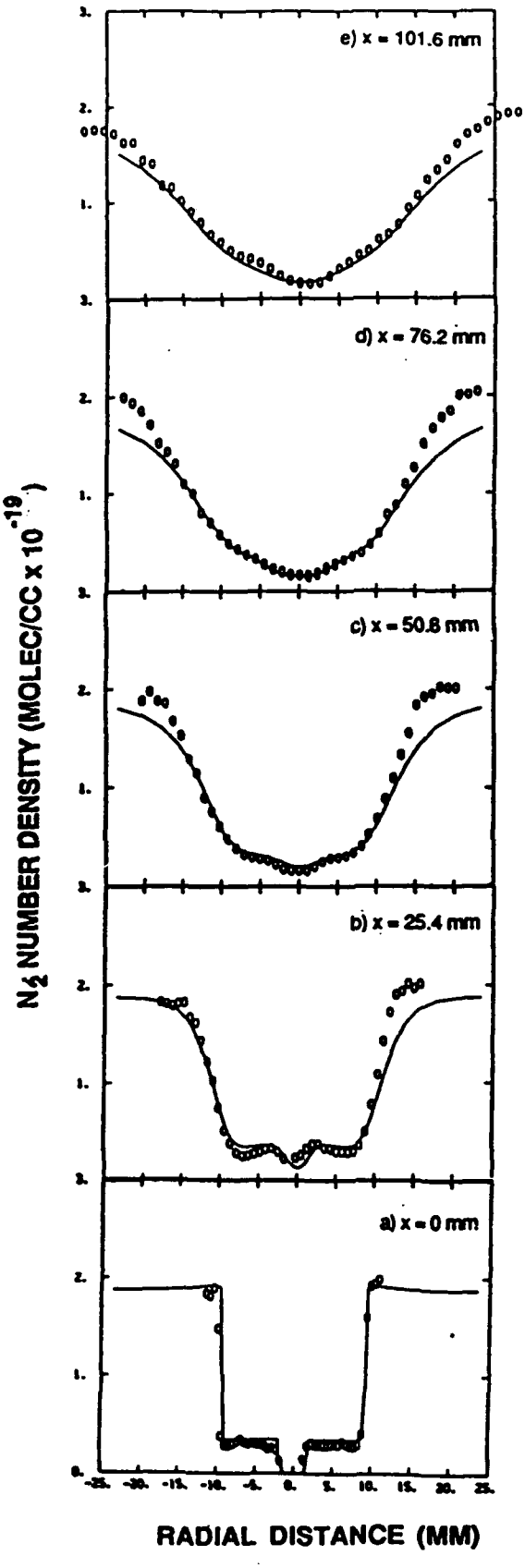

Figure 6. Jarrett SSB Simulation - N_2 Number Density, 101 x 101 Grid.

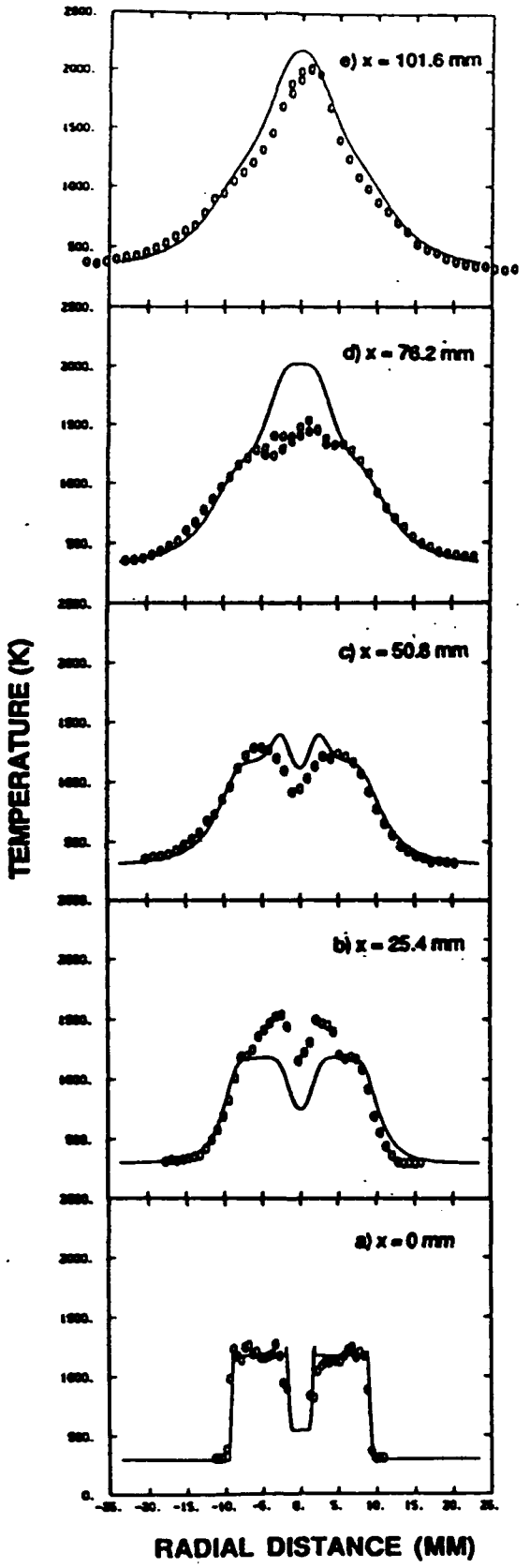

Figure 7. Jarrett SSB Simulation - Temperature, 101 x 61 Grid.

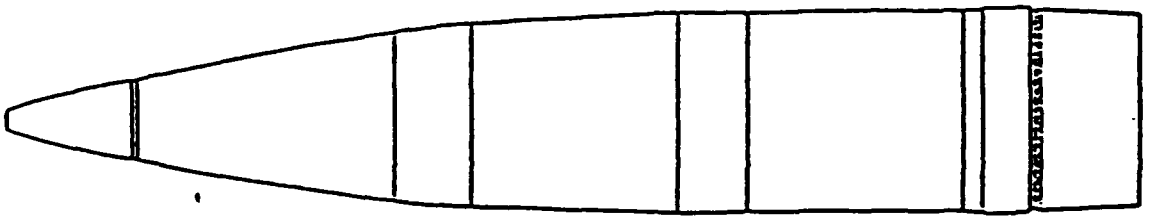

DIMENSIONS

LENGTH OF PROJECTILE	CALIBERS	5.79
NOSE LENGTH	CALIBERS	3.42
CYLINDER LENGTH	CALIBERS	1.80
BOATTAIL LENGTH	CALIBERS	0.50
BOATTAIL ANGLE	DEGREES	3.00

Figure 8. Projectile Schematic (from Danberg, 1990).

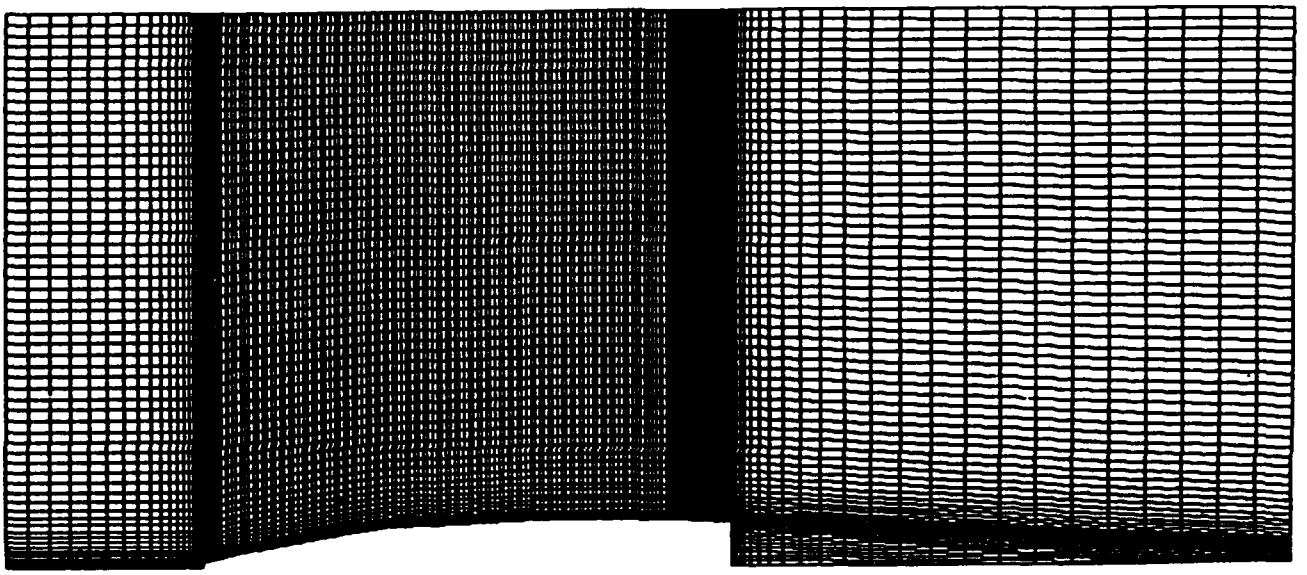

Figure 9. Grid for M864 Projectile with Flat Nose and Flat Base.

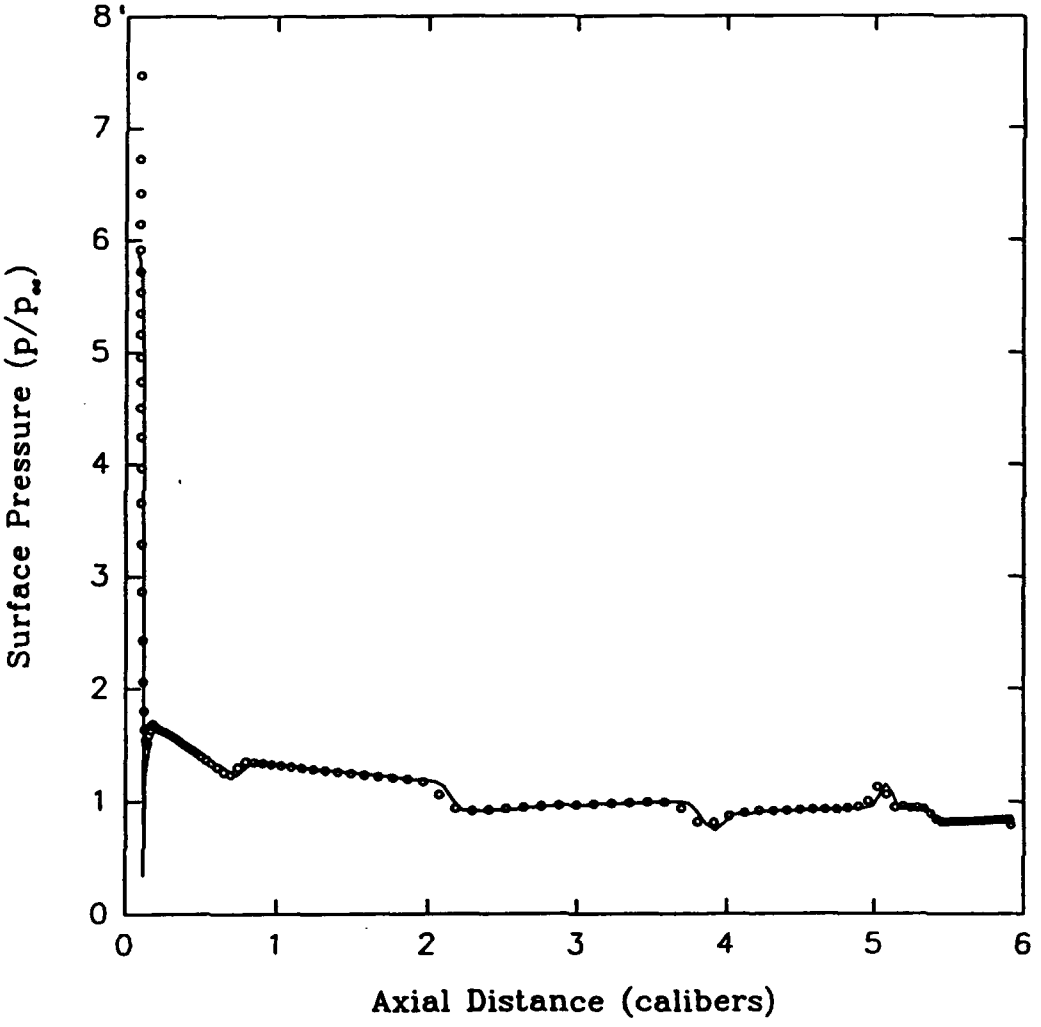

Figure 10. Forebody Surface Pressure Distribution for M864 Projectile *with Flat Nose*, 150 x 280 Grid. Symbols from BRL Calculation.

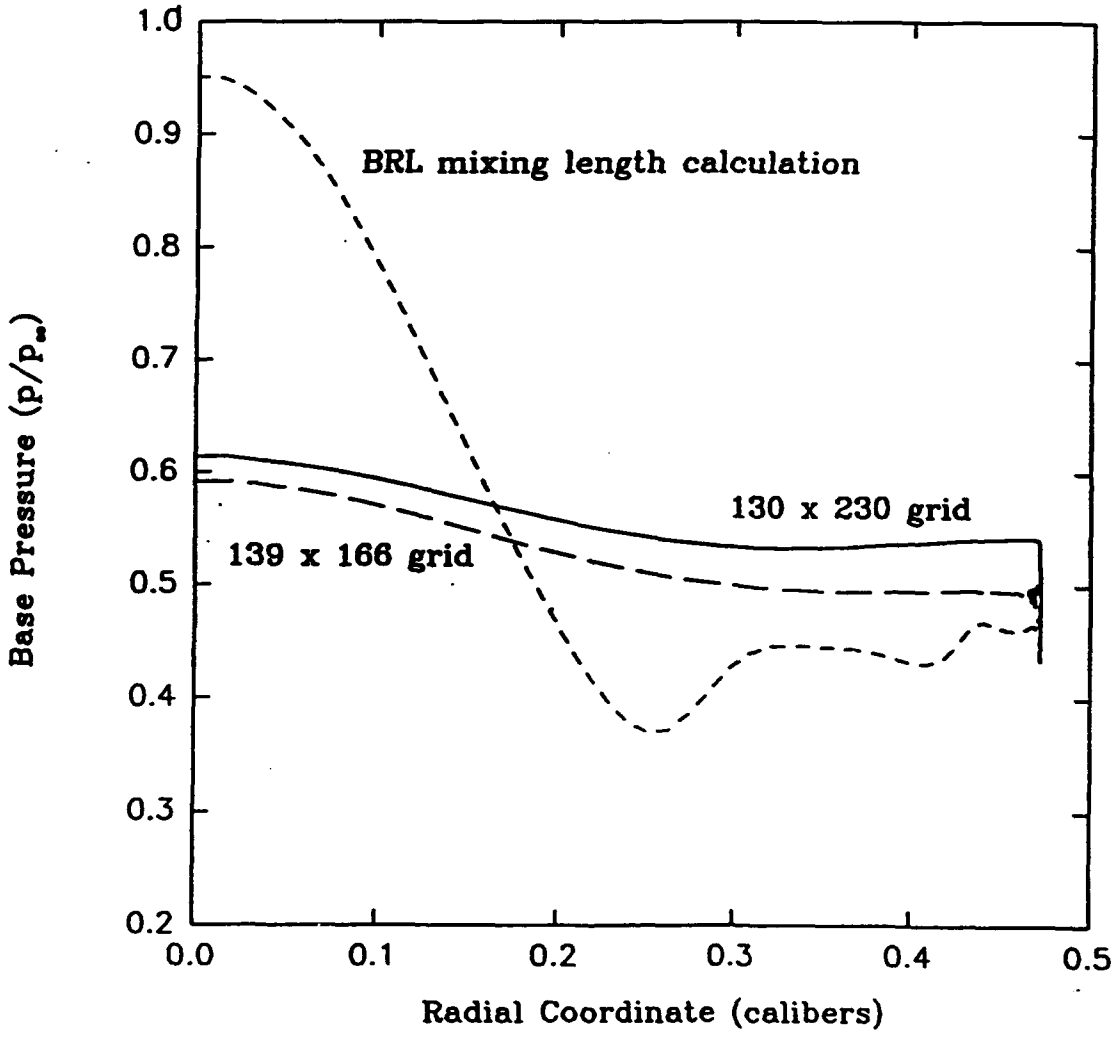

Figure 11. Base Pressure Distributions for Flat Base M864 Projectile. Present Results with k-ε Turbulence Model .

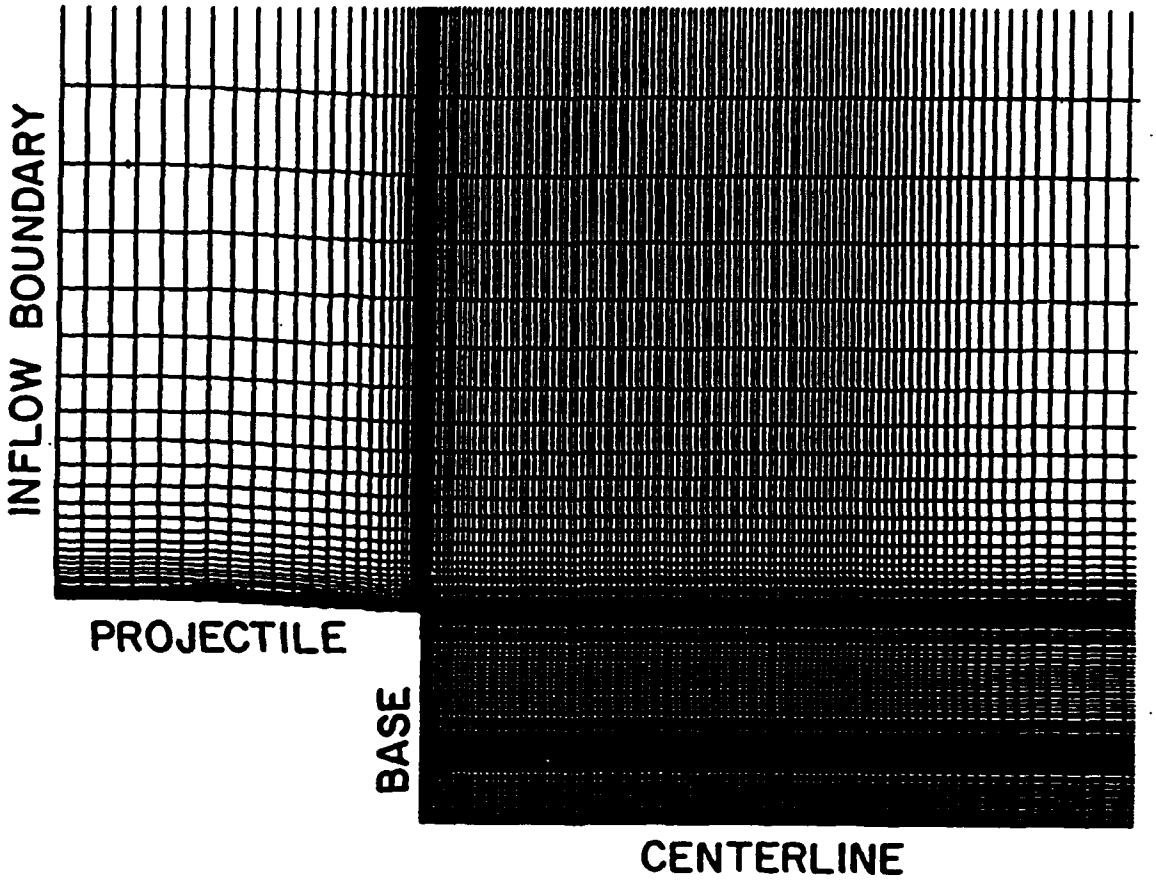

Figure 12. 169 x 196 Grid for M864 Flat Base Projectile for Region Near the Base.

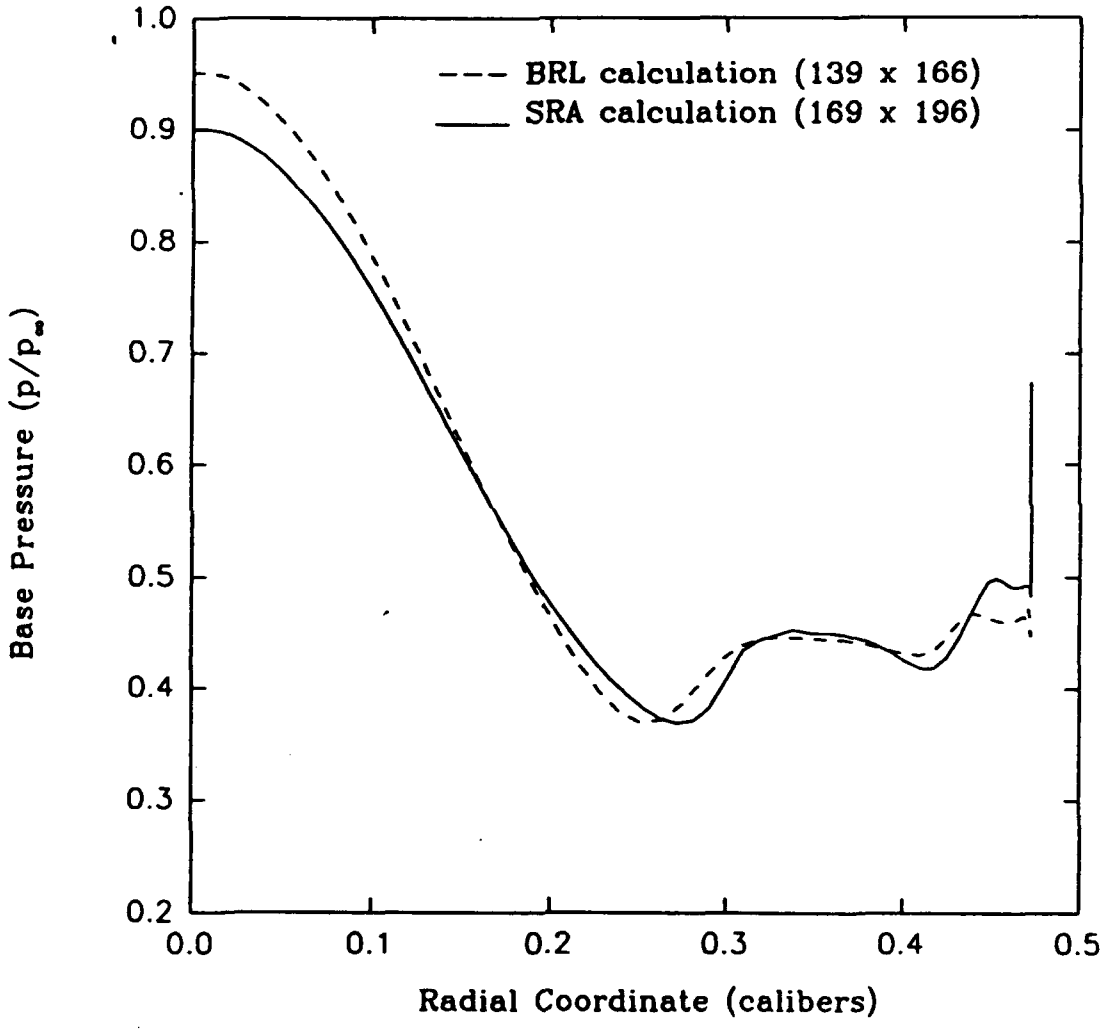

Figure 13. Comparison of BRL and SRA Base Pressure Distributions for Flat Base M864 Projectile without Base Injection .

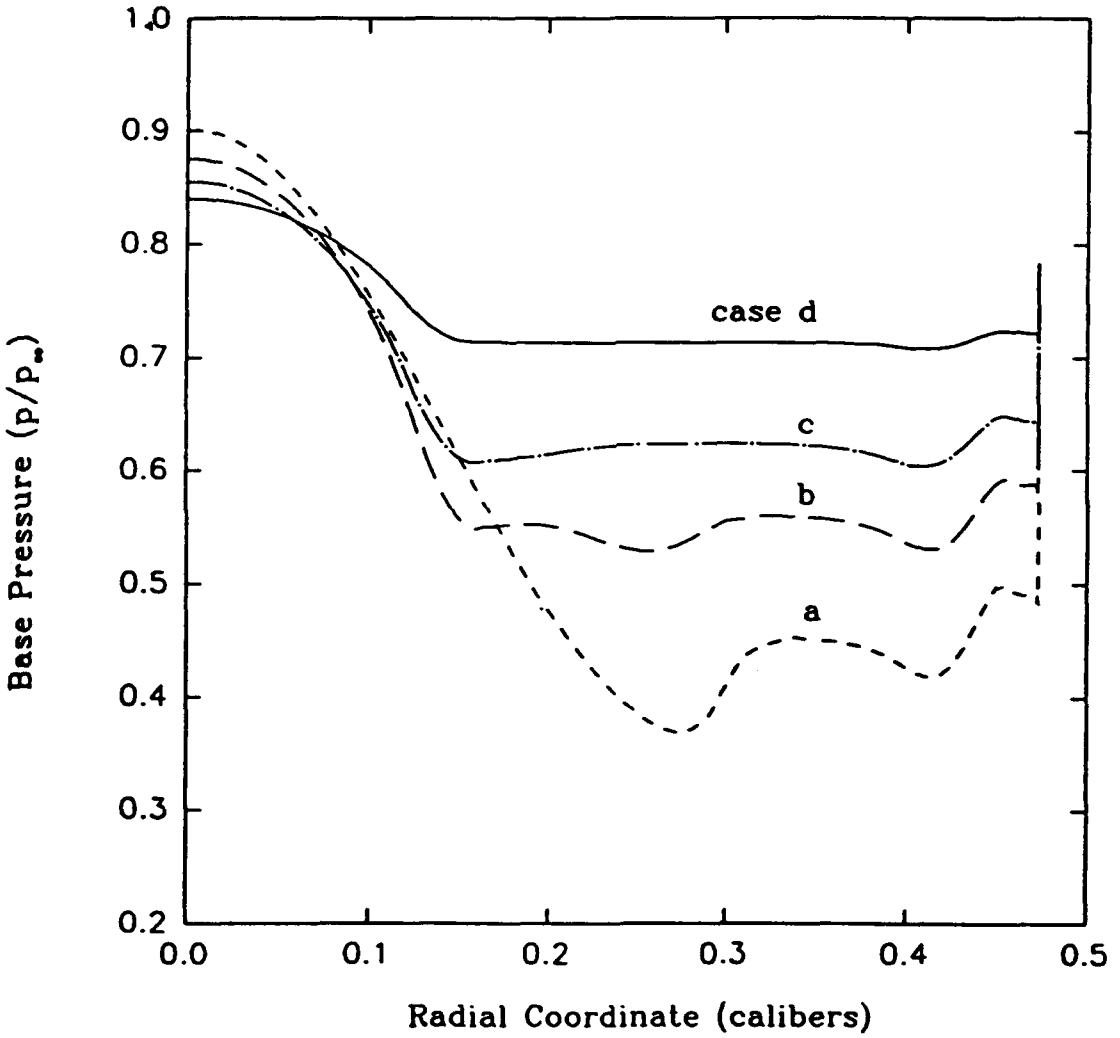

Figure 14. Base Pressure Distributions for Cases a-d with Baldwin-Lomax/Chow Turbulence Model .

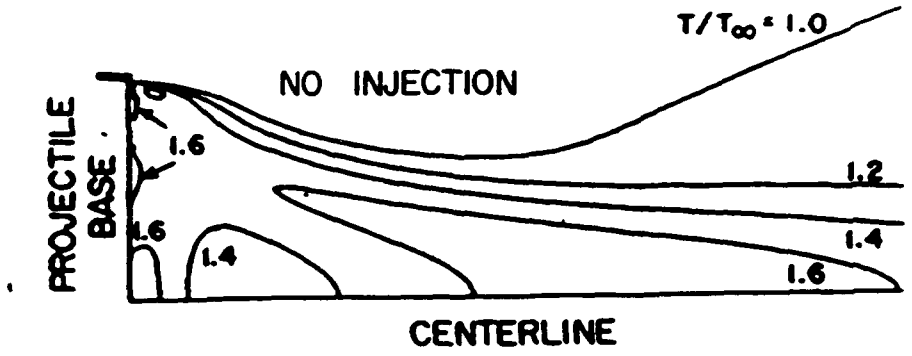

Figure 15a. Temperature Contours for Case (a): $M_\infty = 2$, $I = 0.0$, $T_\infty = 294$ K, $T_W = 294$ K.

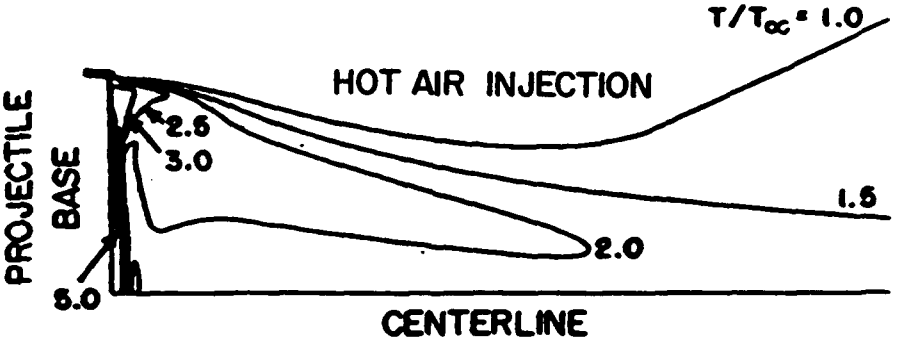

Figure 15b. Temperature Contours for Case (b): Hot Air Injection, $M_\infty = 2$, $I = 0.0022$, $T_\infty = 294$ K, $T_W = 294$ K, $T_{O\ inj} = 1533$ K.

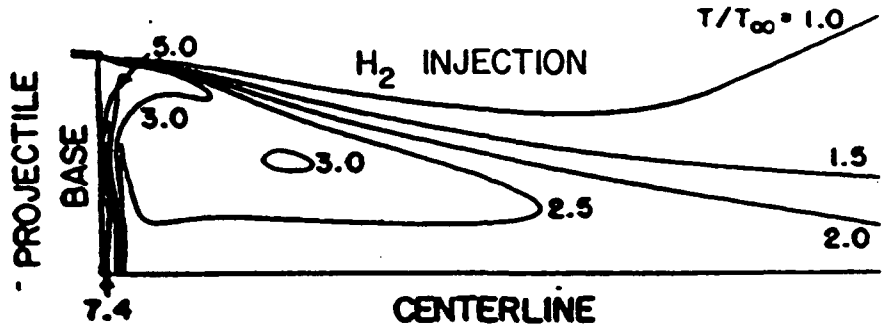

Figure 15c. Temperature Contours for Case (c): H_2 Injection, $M_\infty = 2$, I = 0.0022, $T_\infty = 294$ K, $T_W = 294$ K, $T_{O\ inj} = 1533$ K.

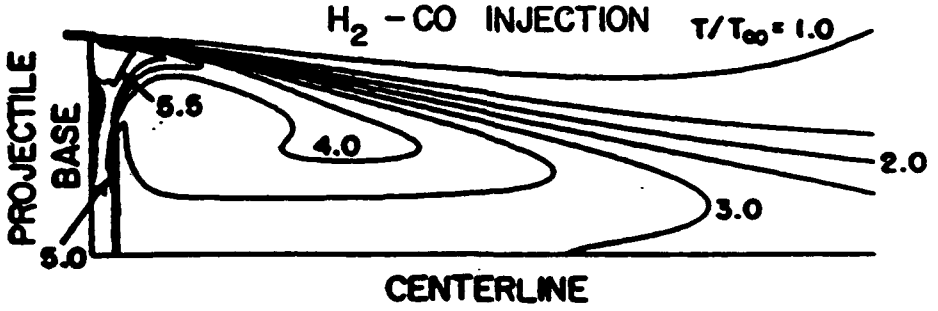

Figure 15d. Temperature Contours for Case (d): H_2-CO Injection, $M_\infty = 2$, I = 0.0022, $T_\infty = 294$ K, $T_W = 294$ K, $T_{O\ inj} = 1533$ K.

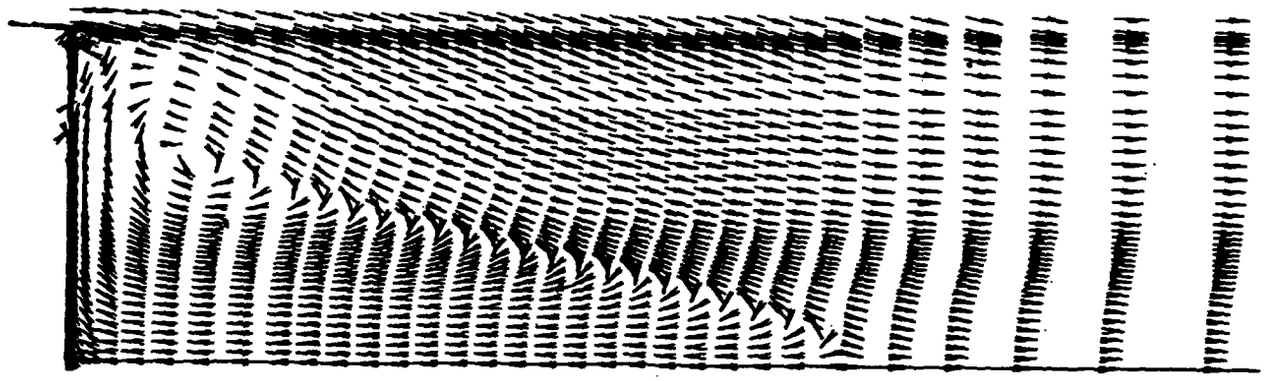

Figure 16a. Velocity Vectors for Case (a): $M_\infty = 2$, $I = 0.0$, $T_\infty = 294$ K, $T_W = 294$ K.

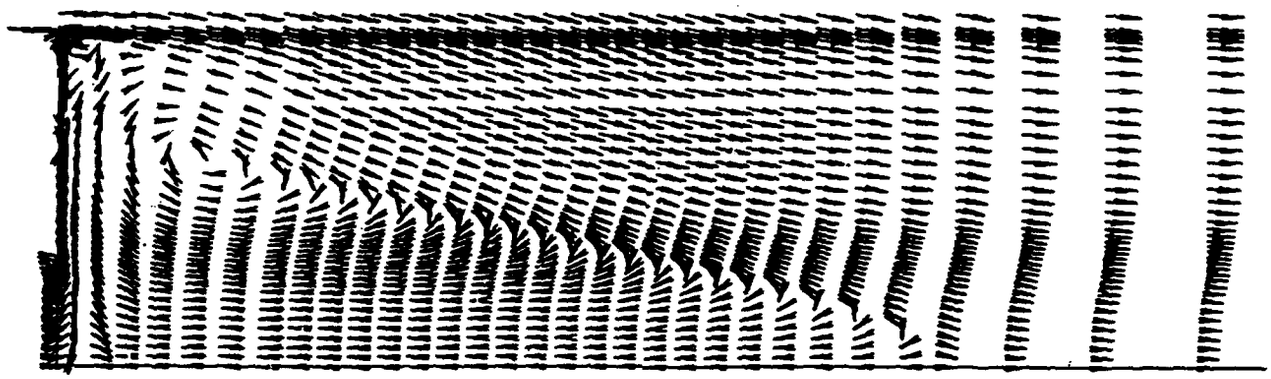

Figure 16b. Velocity Vectors for Case (b): Hot Air Injection, $M_\infty = 2$, $I = 0.0022$, $T_\infty = 294$ K, $T_W = 294$ K, $T_{O\ inj} = 1533$ K.

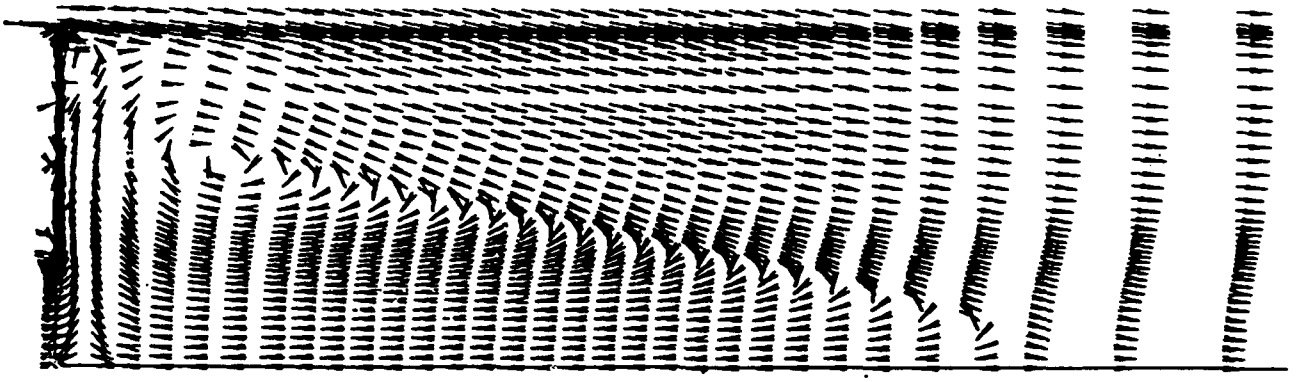

Figure 16c. Velocity Vectors for Case (c): H_2 Injection, $M_\infty = 2$, I = 0.0022, $T_\infty = 294$ K, $T_W = 294$ K, $T_{0\ inj} = 1533$ K.

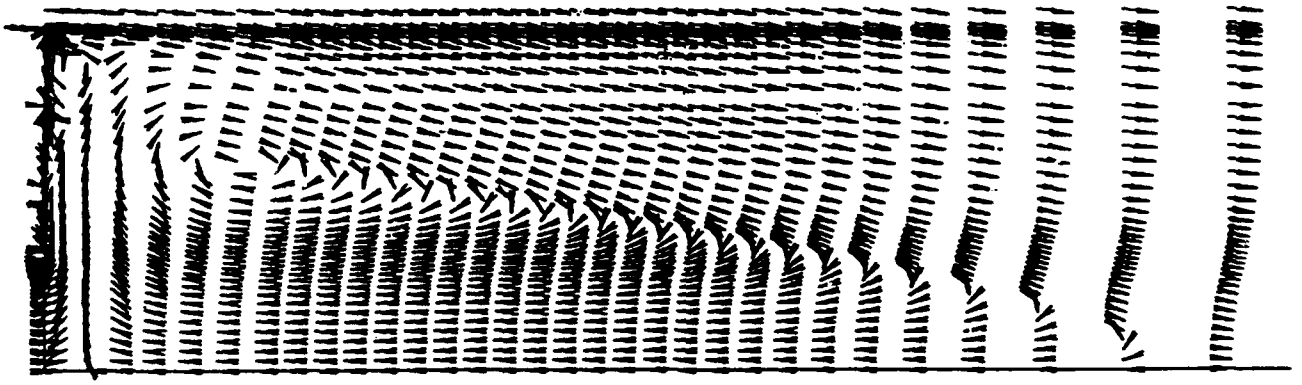

Figure 16d. Velocity Vectors for Case (d): H_2-CO Injection, $M_\infty = 2$, I = 0.0022, $T_\infty = 294$ K, $T_W = 294$ K, $T_{0\ inj} = 1533$ K.

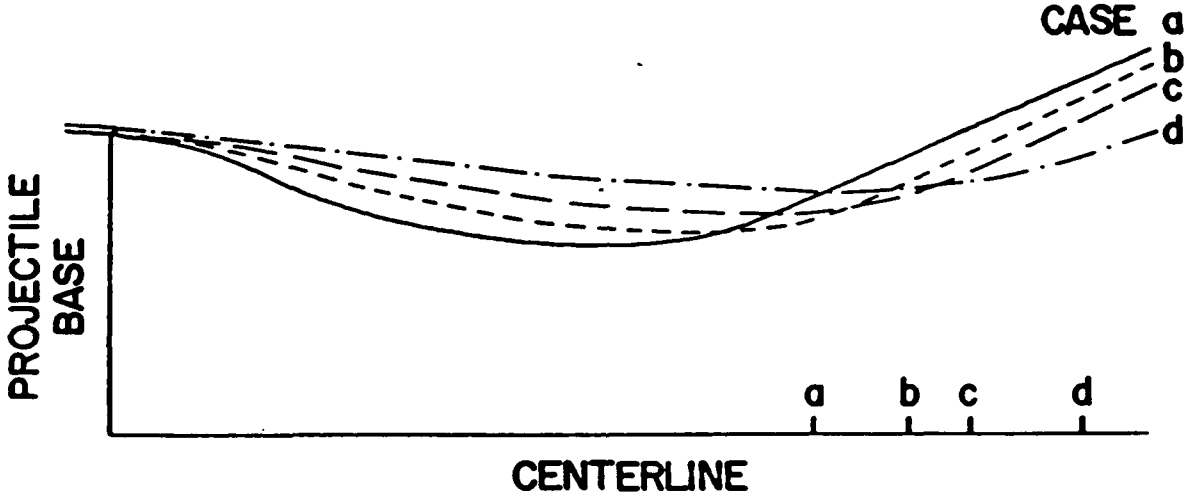

Figure 17. Free Stream Temperature Contours and Rear Stagnation Points for Cases (a, b, c, d).

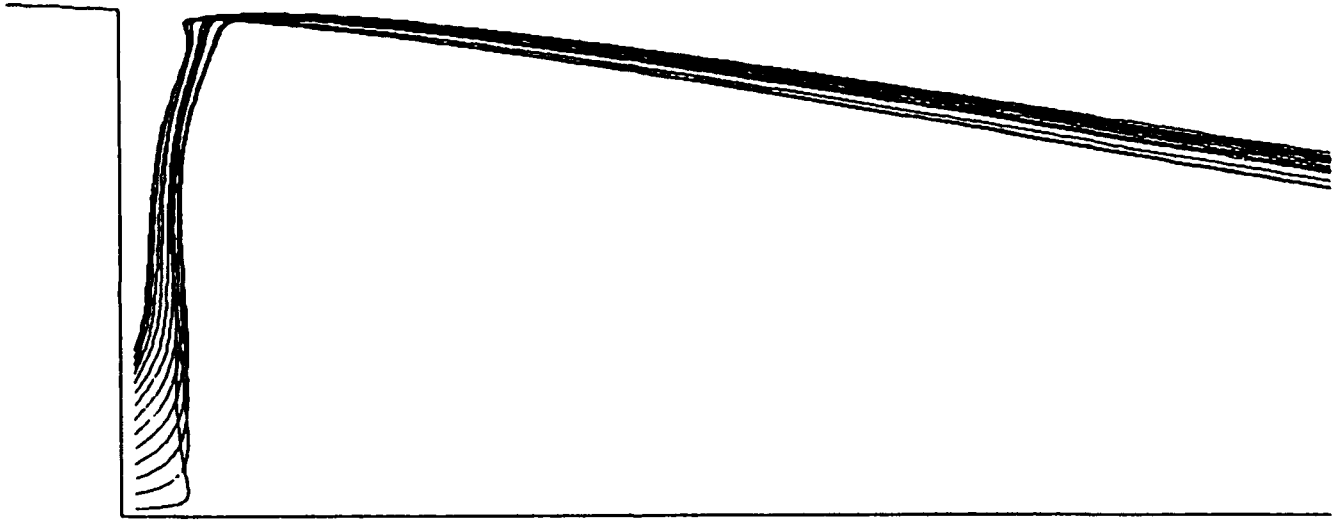

Figure 18. Representative Particle Traces for Two-Phase Reacting Flow.

7. REFERENCES

Baker, W. T., Davis, T. and Matthews, S. E., "Reduction of Drag of a Projectile in a Supersonic Stream by the Combustion of Hydrogen in the Turbulent Wake," APL Report CM-637, Applied Physics Lab., Johns Hopkins University, 1951.

Baldwin, B.S. and Lomax, H., "Thin Layer Approximation and Algebraic Model for Separated Turbulent Flows," AIAA Paper 78-257, January 1978.

Briley, W. R. and McDonald, H., "Solution of the Multidimensional Compressible Navier-Stokes Equations by a Generalized Implicit Method," Journal of Comp. Physics, Vol. 24, pp. 372-397, 1977.

Briley, W. R. and McDonald, H., "On the Structure and Use of Linearized Block Implicit Schemes," Journal of Comp. Physics, Vol. 34, No. 1, pp. 54-72, January 1980.

Cheng, T. S., Wehrmeyer, J. A., Pitz, R. W., Jarrett, O. Jr. and Northam, G. B., "Finite-Rate Chemistry Effects in a Mach 2 Reacting Flow," AIAA Paper No. 91-2320, 27th Joint Propulsion Conference, Sacramento, CA, June 1991.

Childs, R. E. and Caruso, S. C., "On the Accuracy of Turbulent Base Flow Predictions," AIAA Paper No. 87-1439, June 1987.

Childs, R. E. and Caruso, S. C., "Assessment of Modeling and Discretization Accuracy for High Speed Afterbody Flows," AIAA Paper No. 89-0531, January 1989.

Chow, W. L., "Improvement on Numerical Computation of the Thin-Layer Navier-Stokes Equation - with Emphasis on the Turbulent Base Pressure of a Projectile in Transonic Flight Condition," Delivery Order 1713, Contract No. DAAG29-81-D-0100, November 1985.

Correa, S. M., Drake, M. C., Pitz, R. W. and Shyy, W., "Prediction and Measurement of a Non-equilibrium Turbulent Diffusion Flame," 20th International Symposium on Combustion, The Combustion Institute, pp. 337-343, 1984.

Crowe, C. T., Sharma, M. P. and Stock, D. E., "The Particle-Source-In Cell (PSI-CELL) Model for Gas Droplet Flows", Journal of Fluids Engineering, Vol. 99, 1977, pp. 325-332.

Danberg, J. E., "Analysis of the Flight Performance of the 155 mm M864 Base Burn Projectile," BRL-TR-3083, U.S. Army Ballistic Research Laboratory, Aberdeen Proving Ground, Maryland, April 1990.

De Jong, F. J., Sabnis, J. S., and McConnaughey, P. K., "A Combined Eulerian-Lagrangian Two-Phase Flow Analysis of SSME HPOTP Nozzle Plug Trajectories: Part I - Methodology", AIAA Paper 89-2347, AIAA/ASME/SAE/ASEE 25th Joint Propulsion Conference, July 1989.

Dryer, F. L., "The High Temperature Oxidation of Carbon Monoxide and Methane in a Turbulent Flow Reactor," AFOSR Report TR-72-1109, March 1972.

Dryer, F. L. and Glassman, I., "High Temperature Oxidation of CO and CH_4," 14th International Symposium on Combustion, The Combustion Institute, pp. 987-1003, 1973.

Dryer, F. L. and Glassman, I., "Combustion Chemistry of Chain Hydrocarbons," in Alternative Hydrocarbon Fuels: Combustion and Chemical Kinetics, edited by C. T. Bowman and J. Birkeland, AIAA Progress in Astronautics and Aeronautics, Vol. 62, pp. 255-306, 1978.

Dukowicz, J. K., "A Particle-Fluid Model for Liquid Sprays", Journal of Comp. Physics, Vol. 35, 1980, pp. 229-253.

Eggers, J. M., "Turbulent Mixing of Coaxial Compressible Hydrogen-Air Jets," NASA TN D-6487, 1971.

Eklund, D. R., Drummond, J. P. and Hassan, H. A., "Calculation of Supersonic Turbulent Reacting Coaxial Jets," AIAA Journal, Vol. 28, No. 9, pp. 1633-1641, 1990.

Evans, J. S. and Schexnayder, C. J., Jr., "Influence of Chemical Kinetics and Unmixedness on Burning in Supersonic Hydrogen Flames," AIAA Journal, Vol. 18, No. 2, pp. 188-193, 1980.

Gardiner, W. C., Jr., editor, Combustion Chemistry, Springer-Verlag, New York, 1984.

Gibeling, H. J., McDonald, H., and Banks, N. E., "An Implicit Numerical Analysis for Two-Dimensional, Two-Phase Turbulent Interior Ballistic Flows", AIAA Paper 83-0561, AIAA 21st Aerospace Sciences Meeting, January 1983.

Gordon, S. and McBride, B. J., "Computer Program for Calculation of Complex Chemical Equilibrium Compositions, Rocket Performance, Incident and Reflected Shocks, and Chapman-Jouguet Detonations," NASA SP-273, Interim Revision, March 1976.

Gosman, A. D. and Ioannides, E., "Aspects of Computer Simulation of Liquid-Fueled Combustors", Journal of Energy, Vol. 7, 1983, pp. 482-490.

Gough, P. S., "Numerical Analysis of a Two-Phase Flow with Explicit Internal Boundaries", IHCR 77-5, Naval Ordnance Station, Indian Head, MD, April 1977.

Hubbartt, J. E., Strahle, W. C. and Neale, D. H., "Mach 3 Hydrogen External/Base Burning," AIAA Journal, Vol. 19, No. 6, pp. 745-749, 1981.

Jachimowski, C. J., "An Analytical Study of the Hydrogen-Air Reaction Mechanism with Application to Scramjet Combustion," NASA TP-2791, 1988.

Janicka, J. and Kollmann, W., "A Two-Variables Formalism for the Treatment of Chemical Reactions in Turbulent H_2-Air Diffusion Flames," 17th International Symposium on Combustion, The Combustion Institute, pp. 421-430, 1979.

Jarrett, O., Jr., Cutler, A. D., Antcliff, R. R., Chitsomboon, T., Dancey, C. L. and Wang, J. A., "Measurements of Temperature, Density, and Velocity in Supersonic Reacting Flow for CFD Code Validation," 25th JANNAF Combustion Meeting, Huntsville, Alabama, October 1988.

Jarrett, O. Jr., Private Communication, June 1991.

Jones, W. P. and Launder, B. E., "The Prediction of Laminarization with a Two-Equation Model of Turbulence," Intl. Journal of Heat and Mass Transfer, Vol. 15, 1972, pp. 301-314.

Kayser, L. D., Kuzan, J. D. and Vasquez, D. N., "Flight Testing for 155mm Base Burn Projectile," BRL-MR-3708, U.S. Army Ballistic Research Laboratory, Aberdeen Proving Ground, Maryland, November 1988 (AD A201107).

Launder, B. E. and Spalding, D. B., "The Numerical Computation of Turbulent Flows," Computer Methods in Applied Mechanics and Engineering, Vol. 3, 1974, pp. 269-289.

Milojevic, D., Borner, Th., and Durst, F., "Prediction of Turbulent Gas-Particle Flows Measured in a Plain Confined Jet", Proc. World Congress on Particle Technology, Part IV, Nurnberg, April 1986, pp. 485-505.

Murthy, S. N. B., Osborn, J. R., Barrows, A. W. and Ward, J. R., editors, Aerodynamics of Base Combustion," AIAA Progress in Astronautics and Aeronautics, Vol. 40, 1976.

Murthy, S. N. B. and Osborn, J. R., "Base Flow Phenomena with and without Injection: Experimental Results, Theories, and Bibliography," in Aerodynamics of Base Combustion," AIAA Progress in Astronautics and Aeronautics, Vol. 40, pp. 7-210, 1976.

Nietubicz, C. J., Pulliam, T. H., and Steger, J. L., "Numerical Solution of the Azimuthal-Invariant Thin-Layer Navier-Stokes Equations," AIAA Journal, Vol. 18, No. 12, pp. 1411-1412, 1980.

Nietubicz, C. J., Inger, G. R. and Danberg, J. E., "A Theoretical and Experimental Investigation of a Transonic Projectile Flowfield," AIAA Journal, Vol. 22, No. 1, pp. 35-41, 1984.

Nietubicz, C. J. and Sahu, J., "Navier-Stokes Computations of Base Bleed Projectiles," Paper No. II-2, First International Symposium on Special Topics in Chemical Propulsion: Base Bleed, Athens, Greece, November 1988.

Nietubicz, C. J. and Heavey, K., Private Communication, U.S. Army Ballistic Research Laboratory, 1990.

Rogers, R. C. and Chinitz, W., "Using a Global Hydrogen-Air Combustion Model in Turbulent Reacting Flow Calculations," AIAA Journal, Vol. 21, No. 4, pp. 586-592, 1983.

Sabnis, J. S., Gibeling, H. J., and McDonald, H., "A Combined Eulerian-Lagrangian Analysis for Computation of Two-Phase Flows", AIAA Paper 87-1419, AIAA 19th Fluid Dynamics, Plasma Dynamics and Lasers Conference, June 1987.

Sabnis, J. S., Choi, S. K., Buggeln, R. C., and Gibeling, H. J., "Computation of Two-Phase Shear Layer Flow Using an Eulerian-Lagrangian Analysis", AIAA Paper 88-3202, AIAA/ASME/SAE/ASEE 24th Joint Propulsion Conference, July 1988.

Sabnis, J. S. and de Jong, F. J., "Calculation of the Two-Phase Flow in an Evaporating Spray Using an Eulerian-Lagrangian Analysis", AIAA Paper 90-0447, AIAA 28th Aerospace Sciences Meeting, January 1990.

Sahu, J. and Nietubicz, C. J., "Numerical Computation of Base Flow for a Missile in the Presence of a Centered Jet," AIAA Paper No. 84-0527, January 1984.

Sahu, J., Nietubicz, C. J. and Steger, J. L., "Navier-Stokes Computations of Projectile Base Flow with and without Base Injection," AIAA Journal, Vol. 23, No. 9, pp. 1348-1355, 1985.

Sahu, J., "Supersonic Flow over Cylindrical Afterbodies with Base Bleed," Report BRL-TR-2742, U.S. Army Ballistic Research Laboratory, Aberdeen Proving Ground, MD, June 1986. Also, AIAA Paper No. 86-0487.

Sahu, J. and Danberg, J. E., "Navier-Stokes Computations of Transonic Flows with a Two-Equation Turbulence Model," AIAA Journal, Vol. 24, No. 11, pp. 1744-1751, 1986.

Scientific Research Associates, CMINT Computer Code User's Manual, Version 5.04, November 1991.

Solomon, A. S. P., Shuen, J.-S., Zhang, Q.-F., and Faeth, G. M., "A Theoretical and Experimental Study of Turbulent Evaporating Sprays", NASA Contractor Report 174760, September 1984.

Spiegler, E., Wolfshtein, W. and Manheimer-Timnat, Y., "A Model of Unmixedness for Turbulent Reacting Flows," Acta Astronautica, Vol. 3, pp. 265-280, 1976.

Strahle, W. C., Hubbartt, J. E. and Walterick, R., "Base Burning Performance at Mach 3," AIAA Journal, Vol. 20, No. 7, pp. 986-991, 1982.

Sturek, W. B., Dwyer, H. A., Kayser, L. D., Nietubicz, C. J., Reklis, R. P. and Opalka, K. O., "Computations of Magnus Effects for a Yawed, Spinning Body of Revolution," AIAA Journal, Vol. 16, No. 7, pp. 687-692, 1978.

Thompson, J. F., "Program EAGLE Numerical Grid Generation System User's Manual," AFATL-TR-87-15, Vols. I-III, March 1987.

Uenishi, K., Rogers, R. C. and Northam, G. B., "Three-Dimensional Numerical Predictions of the Flow Behind a Rearward-Facing Step in a Supersonic Combustor," AIAA Paper No. 87-1962, July 1987.

Vincenti, W. G. and Kruger, C. H., Jr., Introduction to Physical Gas Dynamics, Wiley, New York, 1965.

Westbrook, C. K., Creighton, J., Lund, C. and Dryer, F. L., "A Numerical Model of Chemical Kinetics of Combustion in a Turbulent Flow Reactor", Journal of Physical Chemistry, Vol. 81, No. 25, pp. 2542-2554, 1977.

White, M. E., Drummond, J. P. and Kumar, A., "Evolution and Application of CFD Techniques for Scramjet Engine Analysis," Journal of Propulsion and Power, Vol. 3, No. 5, 1987.

Intentionally Left Blank

LIST OF SYMBOLS

A	Area
A_D	Maximum Projectile Cross-Sectional Area
A_r	Arrhenius Constant for Reaction r
$\underline{\underline{A}}$	See Eq. (48)
A_{ij}	Element of Time Derivative Matrix
$\hat{A}_{ij}$	See Eq. (49)
A_{base}	Area of Projectile Base
b_r	Temperature Constant for Reaction r
C	Defined by Eq. (A-12)
C_{cp}	Factor for Baldwin-Lomax Turbulence Model
C_{DB}	Base Drag Coefficient
C_{kleb}	Factor for Baldwin-Lomax Turbulence Model
C_p	Frozen Specific Heat
$C_{pi}(T)$	Specific Heat Per Unit Mass of Species i
$\hat{c}_{pi}$	Molar Specific Heat of Species i
C_s	Scaling Parameter; Eq. (50)
C_{wk}	Factor for Baldwin-Lomax Turbulence Model
C_μ	Constant in Jones-Launder Turbulence Model
C_1	Constant in Jones-Launder Turbulence Model
C_2	Constant in Jones-Launder Turbulence Model
D	Diffusion Coefficient; Maximum Projectile Diameter
$\underline{\underline{D}}$	Nonlinear Spatial Difference Operator Matrix
D_ℓ	van Driest Damping Factor
e_{ij}	Rate of Strain Tensor
E_r	Activation Energy of Reaction r
F	Factor for Baldwin-Lomax Turbulence Model
F_i	Conditioning Factor; Eq. (50)
F_i	See Eq. (A-7)
f_i	Mass Fraction of Species i in AP Particle; Eq. (51)
G_i	See Eq. (A-8)
$H(\phi)$	Time Term Vector

h	Enthalpy Per Unit Mass
h_o	Stagnation Enthalpy
h_{fi}	Heat Formation Per Unit Mass of Species i
$h_i(T)$	Enthalpy Per Unit Mass of Species i
$\hat{h}_i^o$	Molar Enthalpy of Species i
I	Injection Parameter
J	Jacobian
J_i	Diffusive Mass Flux at Species i
K	Constant in Baldwin-Lomax Turbulence Model
k	Turbulence Kinetic Energy
$k_{b,r}$	Backward Rate Constant for Reaction r
$K_{c,r}$	Equilibrium Constant for Reaction r
$k_{f,r}$	Forward Rate Constant for Reaction r
$\mathcal{L}$	See Eq. (48)
ℓ	Total Number of Species; Prandtl Mixing Length
m_i	Injection Mass Flow Rate; Rate of Production of Species i Due to Chemical Reaction
$\dot{m}_v$	Particle Vaporization Rate
N_s	Total Number of Species in the System
n	Power for Cartesian and Cylindrical Polar Coordinates
p	Pressure
p_1	See Eq. (A-9)
P_o	Reference Pressure - 1 atm
Pr	Molecular (laminar) Prandtl Number
Pr_T	Turbulent Prandtl Number
q	Multicomponent Energy Flux
q_d	Interdiffusional Energy Flux
Re_p	Particle Reynold's Number; Eq. (54)
R_l	Width Parameter for Eggers Turbulence Model
R_p	Particle Radius
$R_{p,t}$	Time Rate of Change of Particle Radius
R_u	Universal Gas Constant
r	Radius
S	Defined by Eq. (A-11)
$S(\phi)$	Source Term Vector

$\hat{S}_i^o$	Molar Entropy of Species i
Sc	Molecular (laminar) Schmidt Number
Sc_T	Turbulent Schmidt Number
Sh	Sherwood Number; Eq. (53)
T	Temperature
T_f	Reference Temperature
T_o	Reference Temperature; 298.15 K
t	time
U	Velocity Vector
U_i	Velocity Component
$\overline{u_i' u_j'}$	Reynolds Stress
u_{diff}	Difference Between Maximum and Minimum Velocity in a Shear Layer
u_τ	Wall Shear Velocity
ν'_{ir} and ν''_{ir}	Stoichiometric Coefficients for Reaction r
W	Defined by Eq. (A-6)
W_i	Molecular Weight of Species i
X_i	Chemical Symbol of Species i
$[X_i]$	Concentration of Species i
$\bar{x}_i$	Cylindrical Polar Coordinates
Y_i	Mass Fraction of Species i
y^j	Computational Coordinate in j-direction
y_n	Distance Normal to the Wall
y^+	Nondimensional Normal Distance
z	Streamwise Distance
β_i	Defined by Eq. (A-5)
γ_i	Defined by Eq. (A-5)
δ	Local Boundary Layer Thickness
ϵ	Dissipation of Turbulence Kinetic Energy
ζ_i	Defined by Eq. (A-5)
θ	Circumferential Angle
κ	von Karman Constant
κ_{eff}	Effective Thermal Conductivity
μ	Molecular or Laminar Viscosity
μ_{eff}	Effective Viscosity

$\hat{\mu}_i^o$	Molar Chemical Potential
μ_T	Turbulent Viscosity
ρ	Mass Density
ρ_p	Particle Density
σ_k	Constant in Jones-Launder Turbulence Model
σ_ϵ	Constant in Jones-Launder Turbulence Model
τ	Stress Tensor
τ_{ij}	Stress Tensor
τ_w	Wall Shear
ϕ	Equivalence Ratio for the Overall Reaction Process
$\vec{\phi}$	Dependent Variable Vector
$\lvert\vec{\omega}\rvert$	Magnitude of Vorticity

Subcripts

i	Species Number; Coordinate Direction
max	Maximum
min	Minimum
r	Reaction Number
s	Species Number
st	Stoichiometric
w	Wall Value
wake	Wake Value
∞	Free Stream

Superscripts

j	Computational Direction
n	Time Step Number

9. APPENDIX A

Governing Equations

The set of governing partial differential equations which are considered are the ensemble-averaged Navier-Stokes equations. Before these equations can be incorporated into a computer code, a coordinate system must be chosen. The governing equations can then be cast in a form reflecting the choice of the coordinate system. The coordinate system for the present calculations must be capable of treating general configurations. Therefore, the governing equations written in a cylindrical-polar coordinate system are transformed with a general Jacobian transformation of the form

$$y^j = y^j(\bar{x}_1,\ \bar{x}_2,\ \bar{x}_3) \tag{A-1}$$

where $(\bar{x}_1, \bar{x}_2, \bar{x}_3) = (r, \theta, z)$ are the original cylindrical polar coordinates. The velocity components remain the components (U_1, U_2, U_3) in the $(\bar{x}_1, \bar{x}_2, \bar{x}_3)$ coordinate directions, respectively. The new independent variables y^j are the computational coordinates in the transformed system. The transformation (A-1) has been utilized in the computer code both with and without the axisymmetric flow assumption.

The governing equations may be transformed into the computational space using the chain rule and, after some manipulation, written in the following compact form:

$$\frac{\partial (JW)}{\partial \tau} = -\sum_{j=1}^{3} \left\{ \frac{\partial}{\partial y^j} \left[Jy^j{}_{,t} W \right] - \sum_{i=1}^{3} \left[\beta_i \frac{\partial}{\partial y^j} \left[Jy^j{}_{,i} F_i \right] \right.\right.$$

$$\left.\left. + \gamma_i \frac{\partial}{\partial y^j} \left[Jy^j{}_{,i} P_i \right] + \zeta_i \frac{\partial}{\partial y^j} \left[Jy^j{}_{,i} G_i \right] \right] \right\} \tag{A-2}$$

$$+ JS + JC$$

where J is the Jacobian of the inverse transformation given by

$$J = \frac{\partial (\bar{x}_1,\ \bar{x}_2,\ \bar{x}_3)}{\partial (y^1,\ y^2,\ y^3)} \tag{A-3}$$

and

$$y^j_{,t} = \frac{\partial y^j}{\partial t} \quad ; \quad y^j_{,i} = \frac{\partial y^j}{\partial \bar{x}_i} \tag{A-4}$$

Further, the coefficients $\beta_i, \gamma_i, \zeta_i$ are given by

$$\begin{aligned} \beta_1 &= \frac{1}{r}, \quad \beta_2 = \frac{1}{r}, \quad \beta_3 = 1 \\ \gamma_1 &= 1, \quad \gamma_2 = \frac{1}{r}, \quad \gamma_3 = 1 \\ \zeta_1 &= \frac{1}{r^m}, \quad \zeta_2 = \frac{1}{r}, \quad \zeta_3 = 1 \end{aligned} \tag{A-5}$$

and m = 1 for all equations except the $\bar{x}_2$-direction momentum equation, for which m = 2. The vector variables used in Eq. (A-2) are defined as

$$\mathbf{W} = \begin{bmatrix} \rho U_1 \\ \rho U_2 \\ \rho U_3 \\ \rho \\ \rho h_o \\ \rho k \\ \rho \epsilon \\ \rho Y_k \end{bmatrix} \tag{A-6}$$

$$\mathbf{F}_i = r^n \begin{bmatrix} \rho U_1 U_i \\ \rho U_2 U_i \\ \rho U_3 U_i \\ \rho U_i \\ \rho h_o U_i \\ \rho k U_i \\ \rho \epsilon U_i \\ \rho Y_k u_i \end{bmatrix} \tag{A-7}$$

$$G_i = \begin{bmatrix} r^n \tau_{i1} \\ r^2 n \tau_{i2} \\ r^n \tau_{i3} \\ 0 \\ -r^n q_i \\ r^n \left[\mu + \frac{\mu_T}{\sigma_k} \right] \gamma_{ik,i} \\ r^n \left[\mu + \frac{\mu_T}{\sigma_\epsilon} \right] \gamma_{i\epsilon,i} \\ r^n \left[\frac{\mu}{Sc} + \frac{\mu_T}{Sc_T} \right] \gamma_i Y_{k,i} \end{bmatrix} \qquad \text{(A-8)}$$

where n = 1 for i = 1 and n = 0 for i = 2, 3.

$$P_i = \begin{bmatrix} p\delta_{i1} \\ p\delta_{i2} \\ p\delta_{i3} \\ 0 \\ 0 \\ 0 \\ 0 \\ 0 \end{bmatrix} \qquad \text{(A-9)}$$

Note that the velocity components (U_1, U_2, U_3) are the cylindrical-polar velocity components, and τ_{ij} is the stress tensor written in cylindrical-polar coordinates. The molecular and turbulent stress tensor may be written as

$$\tau_{ij} = 2\mu_{eff}\, \bar{e}_{ij} - \frac{2}{3}\mu_{eff}\, (\nabla \cdot U)\delta_{ij} \qquad \text{(A-10)}$$

where $\bar{e}_{ij}$ are components of the rate of strain tensor in cylindrical-polar coordinates. The multicomponent energy flux, q_i, is given by Eq. (7) of the main text.

Finally, the vector S contains source terms and certain differential terms which do not

conform to the basic structure of Eq. (A-2), and the vector C contains the additional curvature terms due to the cylindrical-polar coordinate system.

$$S = \begin{bmatrix} \dot{m}_v \\ 0 \\ 0 \\ 0 \\ \frac{\partial p}{\partial t} + \nabla \bullet (\tau \cdot U) \\ 2\mu_T \left[\bar{e}_{ij} \, \bar{e}_{ij} \right] - \rho\epsilon - 2\rho\nu \left[\Delta k^{\frac{1}{2}} \right]^2 \\ c_1 \frac{\epsilon}{k} \mu_T \left[2\bar{e}_{ij} \, \bar{e}_{ij} \right] + \frac{2\mu\mu_T}{\rho} \left[\nabla^2 U \right]^2 - c_2 \rho \frac{\epsilon^2}{k} \\ m_k \end{bmatrix} \qquad \text{(A-11)}$$

$$C = \begin{bmatrix} \frac{1}{r} \rho U_2^{\,2} - \frac{1}{r} \tau_{22} \\ -\frac{1}{r} \rho U_1 U_2 \\ 0 \\ 0 \\ 0 \\ 0 \\ 0 \\ 0 \end{bmatrix} \qquad \text{(A-12)}$$

The chemical source term, m_k, is determined from Eqs. (17) and (22),

$$m_k = W_k \frac{d[X_k]}{dt} \qquad \text{(A-13)}$$

No. of Copies	Organization
2	Administrator Defense Technical Info Center ATTN: DTIC-DDA Cameron Station Alexandria, VA 22304-6145
1	Commander U.S. Army Materiel Command ATTN: AMCAM 5001 Eisenhower Ave. Alexandria, VA 22333-0001
1	Director U.S. Army Research Laboratory ATTN: AMSRL-D 2800 Powder Mill Rd. Adelphi, MD 20783-1145
1	Director U.S. Army Research Laboratory ATTN: AMSRL-OP-CI-A, Tech Publishing 2800 Powder Mill Rd. Adelphi, MD 20783-1145
2	Commander U.S. Army Armament Research, Development, and Engineering Center ATTN: SMCAR-IMI-I Picatinny Arsenal, NJ 07806-5000
2	Commander U.S. Army Armament Research, Development, and Engineering Center ATTN: SMCAR-TDC Picatinny Arsenal, NJ 07806-5000
1	Director Benet Weapons Laboratory U.S. Army Armament Research, Development, and Engineering Center ATTN: SMCAR-CCB-TL Watervliet, NY 12189-4050
(Unclass. only)1	Commander U.S. Army Rock Island Arsenal ATTN: SMCRI-TL/Technical Library Rock Island, IL 61299-5000
1	Director U.S. Army Aviation Research and Technology Activity ATTN: SAVRT-R (Library) M/S 219-3 Ames Research Center Moffett Field, CA 94035-1000

No. of Copies	Organization
1	Commander U.S. Army Missile Command ATTN: AMSMI-RD-CS-R (DOC) Redstone Arsenal, AL 35898-5010
1	Commander U.S. Army Tank-Automotive Command ATTN: ASQNC-TAC-DIT (Technical Information Center) Warren, MI 48397-5000
1	Director U.S. Army TRADOC Analysis Command ATTN: ATRC-WSR White Sands Missile Range, NM 88002-5502
1	Commandant U.S. Army Field Artillery School ATTN: ATSF-CSI Ft. Sill, OK 73503-5000
(Class. only)1	Commandant U.S. Army Infantry School ATTN: ATSH-CD (Security Mgr.) Fort Benning, GA 31905-5660
(Unclass. only)1	Commandant U.S. Army Infantry School ATTN: ATSH-CD-CSO-OR Fort Benning, GA 31905-5660
1	WL/MNOI Eglin AFB, FL 32542-5000
	Aberdeen Proving Ground
2	Dir, USAMSAA ATTN: AMXSY-D AMXSY-MP, H. Cohen
1	Cdr, USATECOM ATTN: AMSTE-TC
1	Dir, ERDEC ATTN: SCBRD-RT
1	Cdr, CBDA ATTN: AMSCB-CI
1	Dir, USARL ATTN: AMSRL-SL-I
10	Dir, USARL ATTN: AMSRL-OP-CI-B (Tech Lib)

No. of Copies Organization

4 Commander
U.S. Army Armament Research, Development and Engineering Center
ATTN: SMCAR-AET-A,
R. Kline
H. Hudgins
S. Kahn
J. Grau
Picatinny Arsenal, NJ 07806-5001

1 Commander
U.S. Army Missile Command
ATTN: AMSMI-RD-SS-AT,
B. Walker
Redstone Arsenal, AL 35898-5010

1 Commander
U.S. Naval Surface Weapons Center
ATTN: Dr. F. Moore
Dahlgren, VA 22448

3 Commander
Naval Surface Weapons Center
ATTN: Code R44,
Dr. F. Priolo
Dr. A. Wardlaw
K24, B402-12, Dr. W. Yanta
White Oak Laboratory
Silver Spring, MD 20903-5000

1 USAF Wright Aeronautical Laboratories
ATTN: AFWAL/FIMG,
Dr. J. Shang
WPAFB, OH 45433-6553

3 Director
National Aeronautics and Space Administration
Langley Research Center
ATTN: Tech Library
Dr. M. J. Hemsch
Dr. J. South
Langley Station
Hampton, VA 23665

No. of Copies Organization

3 Director
National Aeronautics and Space Administration
Ames Research Center
ATTN: MS-227-8, L. Schiff
MS-258-1,
T. Holst
D. Chaussee
Moffett Field, CA 94035

1 Massachusetts Institute of Technology
ATTN: Tech Library
77 Massachusetts Avenue
Cambridge, MA 02139

3 Sandia National Laboratories
ATTN: Dr. Daniel Barnette
Dr. W. Oberkampf
Dr. F. Blottner
Division 1554
P.O. Box 5800
Albuquerque, NM 87185

1 University of California, Davis
Department of Mechanical Engineering
ATTN: Prof. H. A. Dwyer
Davis, CA 95616

1 VRA Inc.
ATTN: Dr. Clark H. Lewis
P.O. Box 50
Blacksburg, VA 24060

1 University of Maryland
Department of Aerospace Engineering
ATTN: Dr. J. D. Anderson, Jr.
College Park, MD 20742

1 University of Texas
Department of Aerospace Engineering and Engineering Mechanics
ATTN: Dr. D. S. Dolling
Austin, TX 78712-1055

1 University of Florida
Department of Engineering Sciences
College of Engineering
ATTN: Prof. C. C. Hsu
Gainesville, FL 32611

No. of

Copies Organization

1 University of Florida
Department of Engineering Sciences
College of Engineering
ATTN: Prof. C. C. Hsu
Gainesville, FL 32611

1 Pennsylvania State University
Department of Mechanical Engineering
ATTN: Dr. Kenneth Kuo
University Park, PA 16802

1 Florida Atlantic University
Department of Mechanical Engineering
ATTN: Dr. W. L. Chow
Boca Raton, FL 33431

1 Georgia Institute of Technology
School of Aerospace Engineering
ATTN: Dr. Warren C. Strahle
Atlanta, GA 30332

1 AEDC
Calspan Field Service
ATTN: Dr. John Benek
MS 600
Tullahoma, TN 37389

1 McDonnell Douglas Corporation
Dept 222 Bldg 110 Lev 1 RM/PT 151
Mail Code 5
ATTN: Dr. Thomas P. Gielda
P.O. Box 516
Saint Louis, MO 63166-0516

1 Visual Computing
ATTN: Jeffrey Q. Cordova
883 N. Shoreline Blvd.
Suite B210
Mountain View, CA 94043

1 MDA Engineering, Inc.
ATTN: John P. Steinbrenner
500 E. Border St.
Suite 401
Arlington, TX 76010

INTENTIONALLY LEFT BLANK.

USER EVALUATION SHEET/CHANGE OF ADDRESS

This Laboratory undertakes a continuing effort to improve the quality of the reports it publishes. Your comments/answers to the items/questions below will aid us in our efforts.

1. ARL Report Number ARL-CR-2 Date of Report November 1992

2. Date Report Received _____

3. Does this report satisfy a need? (Comment on purpose, related project, or other area of interest for which the report will be used.) _____

4. Specifically, how is the report being used? (Information source, design data, procedure, source of ideas, etc.) _____

5. Has the information in this report led to any quantitative savings as far as man-hours or dollars saved, operating costs avoided, or efficiencies achieved, etc? If so, please elaborate. _____

6. General Comments. What do you think should be changed to improve future reports? (Indicate changes to organization, technical content, format, etc.) _____

CURRENT ADDRESS

_____
Organization

_____
Name

_____
Street or P.O. Box No.

_____
City, State, Zip Code

7. If indicating a Change of Address or Address Correction, please provide the Current or Correct address above and the Old or Incorrect address below.

OLD ADDRESS

_____
Organization

_____
Name

_____
Street or P.O. Box No.

_____
City, State, Zip Code

(Remove this sheet, fold as indicated, staple or tape closed, and mail.)

DEPARTMENT OF THE ARMY

OFFICIAL BUSINESS

BUSINESS REPLY MAIL
FIRST CLASS PERMIT No 0001, APG, MD

Postage will be paid by addressee

Director
U.S. Army Research Laboratory
ATTN: AMSRL-OP-CI-B (Tech Lib)
Aberdeen Proving Ground, MD 21005-5066

NO POSTAGE
NECESSARY
IF MAILED
IN THE
UNITED STATES